

Seismoelectromagnetic waves radiated by a double couple source in a saturated porous medium

Yongxin Gao¹ and Hengshan Hu^{1,2}

¹Department of Astronautics and Mechanics, Harbin Institute of Technology, Postbox 344, 92, West Dazhi Street, Harbin 150001, China.

E-mail: wave_hu@yahoo.com

²State key lab of advanced welding production technology, Harbin Institute of Technology, Postbox 436, 92, West Dazhi Street, Harbin 150001, China

Accepted 2010 January 16. Received 2009 December 9; in original form 2009 September 24

SUMMARY

Studied in this paper are the properties of seismoelectromagnetic waves radiated by a double couple in a saturated porous medium arising from the electrokinetic effect. First, using the Pride's equations, we derive the Green's function of the magnetic field due to a single point force as a complement of previous authors' works, in which only the Green's functions of the solid displacement, the relative fluid–solid displacement and the electric field were expressed. Furthermore, we extend these Green's functions to cater for the moment tensor sources. Then we derive the Green's functions of the solid displacement, the electric and magnetic fields in the frequency-space domain excited by a double couple source, which is frequently used in earthquake seismology. To visualize these fields, the radiation patterns are calculated and displayed. The results illustrate that the radiation pattern of the electric far field for the longitudinal (or transverse) wave is the same in shape as that of the far field of the *P* (or *S*) wave in elastodynamics. For a transverse wave, the electric and magnetic far fields share the same radiation patterns in shape, while the electric and magnetic near fields do not. For each of the four body waves, the far, intermediate and near fields are compared at different receiver-to-source distances, respectively. The electromagnetic (EM) wave has a much longer near-field-dominating distance than the seismic waves. We calculate the waveforms in the time–space domain by numerically Fourier transforming the Green's functions into the time domain. In order to validate these Green's functions and the waveforms, we calculate the waveforms again by another method. The main idea of the method is regarding the source as a displacement–stress–EM discontinuity vector. The result shows that the waveforms from those two methods are in excellent agreement. In the waveforms, there are the electric fields accompanying both the *P* and *S* waves, as well as the magnetic field accompanying the *S* wave. We testify that the *S* wave generally has a weaker capacity than the *P* wave in inducing an electric field. In the waveforms, there is also an independently propagating EM wave, which has a much higher speed than the seismic waves, and reaches the observation point immediately after the source launched. By comparing the waveforms at different receiving locations, we find that waveforms differ at different observation orientations.

Key words: Magnetic and electrical properties; Body waves; Theoretical seismology; Wave propagation.

1 INTRODUCTION

It is known that seismic waves can induce electromagnetic (EM) fields. The coupling between the seismic and EM energies may result from the electrokinetic effect (Thompson & Gist 1993; Butler *et al.* 1996; Mikhailov *et al.* 1997; Garambois & Dietrich 2001), the piezoelectric effect (Huang 2002), the EM induction effect (Matsushima *et al.* 2002), and some other mechanisms. Among these mechanisms, the electrokinetic phenomenon has stirred great interest of geophysicists during the past decades. As early as in 1939 Ivanov measured the electric field induced by the seismic waves. To explain the phenomena appeared in Ivanov's field experiment, Frenkel (1944) built a mathematical model to analyse the electric field induced by a seismic wave by assuming the existence of the electric double layer on the solid–fluid interface in a porous medium. In recent years, successful field and laboratory experiments (e.g. Thompson & Gist 1993; Zhu *et al.* 1994, 1999, 2008; Butler *et al.* 1996; Mikhailov *et al.* 1997; Garambois & Dietrich 2001; Bordes *et al.* 2006, 2008) provided further evidences for the electrokinetic

phenomenon and excited more interest among scientists. The electrokinetic effect has been recognized as a potential tool for explorations (Thompson & Gist 1993; Butler *et al.* 1996; Mikhailov *et al.* 1997; Garambois & Dietrich 2001).

As a development of Frenkel's work, Pride (1994) derived a set of macroscopic equations governing the coupled poroelastic and EM field. In brief, in his set of equations the Biot's poroelastodynamic equations are coupled to the Maxwell's equations of electrodynamics. As the coupling coefficient is experimentally measurable (Pengra *et al.* 1999; Reppert & Morgan 2002), Pride's equations can be used to quantitatively model the electrokinetic coupling phenomena. From the plane wave solutions to Pride's equations (Pride & Haartsen 1996), it is clear that there are two kinds of EM fields. One is local and restricted to the seismic disturbance region. The other is a propagating wave. When a seismic wave propagates through a porous medium, a relative fluid–solid motion is induced. The relative fluid–solid motion transports the ions in the pore fluid to cause local EM field due to the existence of the electric double layer. Such a local EM field does not exist outside of the seismic wave pulse and is thus an accompanying EM field. This is the first kind of EM disturbance, which can be regarded as local material response. The second kind of EM disturbance happens when the seismic wave crosses an interface separating two porous media with different properties. An independently propagating EM wave is then generated at this interface. Such an EM wave is much faster than the seismic wave. Those two effects were illustrated in detail by the numerical simulations of Haartsen & Pride (1997) and Garambois & Dietrich (2002). These theoretical simulations can partly explain the observations made by Thompson & Gist (1993) and Garambois & Dietrich (2001). For well logging cases, analytic and numerical methods were performed to describe the EM fields induced in the borehole embedded in a porous medium (Hu & Liu 2002; Hu *et al.* 2007; Guan & Hu 2008; Guan *et al.* 2009).

Previous works mentioned above mostly focused on the application of the electrokinetic effect for the exploration purpose. However, electrokinetic effect may also be active in earthquake seismology, and is a possible mechanism for the existence of the coseismic EM disturbances. In recent years, coseismic EM signals have been measured before, during or after earthquakes. Many articles have been published to analyse these recorded coseismic EM signals. Huang (2002) developed a physical model considering the compensation of piezoelectric effect and the dislocation theory of fault. He suggested the piezoelectric effect may be a possible mechanism of the recorded seismoelectric signals during the 1995 $M = 7.2$ Kobe earthquake. Matsushima *et al.* (2002) supposed the electrically conducting crust that vibrates under the Earth's magnetic field may make motional EM induction. They called this mechanism the seismo-dynamo effect. By estimating the motional EM response using the magnetotelluric fields and ground motion observed during the 1999 $M_w = 7.4$ İzmit earthquake aftershock ($M = 4.5$), they thought that the seismo-dynamo effect is a plausible mechanism for the variations in the magnetotelluric fields associated with the seismic waves. Honkura *et al.* (2002) studied the small electric and magnetic signals before the seismic waves during the 1999 $M_w = 7.4$ İzmit earthquake, but they did not give a reasonable explanation for the existence of these signals. Karakelian *et al.* (2002) analysed the ultralow-frequency EM field measurement associated with the 1999 $M = 7.1$ Hector Mine earthquake sequence. They thought that the coseismic EM fields are perhaps due to the electrokinetic effect. Tang *et al.* (2008) also supposed that the coseismic EM fields associated with the aftershock of the M_s 8.0 Wenchuan earthquake are possibly caused by the electrokinetic effect. Regrettably, Karakelian *et al.* (2002) and Tang *et al.* (2008) haven't provided any evidence for their supposition. However, since the seismoelectric and seismomagnetic conversions arising from the electrokinetic effect assuredly exist and are measurable (Bordes *et al.* 2006, 2008), the electrokinetic effect in an earthquake incident deserves our in-depth study.

As is known, most natural earthquakes were caused by the fault slips. Pride *et al.* (2004) and Pride & Garambois (2005) studied the electric response in a uniform porous crust following a shear dislocation on an internal slip surface. They considered a finite fault model and investigated how the fluid-pressure equilibration affects both the stress state and the electric fields near the fault in months following an earthquake. In their modelling, the fluid pressure diffusion process was seen as a very low frequency ($f < 0.01$ Hz) slow P wave. And they suggested monitoring the diffusion process by observing the electric field induced by the slow P wave. However, they focused on the effect of the slow P wave and did not discuss the magnetic field. In this paper, we study both the electric and magnetic fields induced by the seismic waves. We study a fault, of which the scale is much smaller than the seismic wavelength considered. Therefore, the wavefields generated by the slip of such a fault are recognized equivalent to those generated by a double couple source. Our goal is to describe the properties of the electric and magnetic fields radiated by such a double couple source. The fundamental solutions, that is, the Green's functions for a uniform infinite porous medium are investigated to reveal the properties of these fields. Over the past decades, Green's functions for wave propagating in a poroelastic solid based on Biot's theory have been presented in various formulations by many authors (e.g. Burridge & Vargas 1979; Norris 1985; Bonnet 1987; Boutin 1991). These various representations of Green's functions were systematically reviewed and discussed by Karpfinger *et al.* (2009). For the coupled poroelastic and EM problem, Green's functions were presented by Pride & Haartsen (1996). However, in Pride & Haartsen (1996)'s work only the Green's functions of the solid displacement \mathbf{u} , the relative fluid–solid displacement \mathbf{w} and the electric field \mathbf{E} were presented, while the Green's function of the magnetic field is lacking. Besides, in their work, only the single point sources were considered, namely, the current-source \mathbf{C} and the single forces acting on the bulk material \mathbf{F} and fluid phase \mathbf{f} , respectively. These single point sources are often insufficient in seismology. As a supplement, in this paper, the moment tensors are used to describe more types of sources.

We organize the present paper as follows. In the coming section, we give a brief introduction of Pride's equations. Next, we review the frequency-space-domain Green's functions of \mathbf{u} , \mathbf{w} and \mathbf{E} due to a single point force that have been obtained by Pride & Haartsen (1996). In addition, we derive the Green's function of the magnetic field \mathbf{H} . In Section 4, we derive the Green's functions of \mathbf{u} , \mathbf{w} , \mathbf{E} and \mathbf{H} relating to the moment tensors. Thereafter, with the help of the radiation patterns, we illustrate the radiation characteristics of the electric and magnetic fields generated by a double couple source. Subsequently, we calculate the full waveforms of the solid displacement, the electric and magnetic fields due to the double couple source by numerically Fourier transforming the corresponding Green's functions into the time–space domain.

Meanwhile, to check the validity of the Green's functions obtained, we introduce another method to calculate the full waveforms again. The main idea of the method is taking the source as a displacement–stress–EM discontinuity vector (Haartsen & Pride 1997; Garambois & Dietrich 2002; White & Zhou 2006). Furthermore, we calculate the waveforms at different locations to investigate the influence of the observation orientation on the received waveforms.

2 PRIDE'S EQUATIONS

Assuming an $e^{-i\omega t}$ time dependence, the equations governing the coupled EM and elastic waves in an isotropic homogeneous porous medium are

$$\nabla \times \mathbf{H} = [\sigma(\omega) - i\omega\epsilon]\mathbf{E} + L(\omega)(-\nabla P + \omega^2\rho_f\mathbf{u} + \mathbf{f}) + \mathbf{C}, \quad (1)$$

$$\nabla \times \mathbf{E} = i\omega\mu\mathbf{H} - \mathbf{M}, \quad (2)$$

$$-\omega^2(\rho\mathbf{u} + \rho_f\mathbf{w}) = \nabla \cdot \boldsymbol{\tau} + \mathbf{F}, \quad (3)$$

$$-i\omega\mathbf{w} = L(\omega)\mathbf{E} + \kappa(\omega)/\eta(-\nabla P + \omega^2\rho_f\mathbf{u} + \mathbf{f}), \quad (4)$$

$$\boldsymbol{\tau} = [(H - 2G)\nabla \cdot \mathbf{u} + C\nabla \cdot \mathbf{w}]\mathbf{I} + G(\nabla\mathbf{u} + \nabla\mathbf{u}^T), \quad (5)$$

$$-P = C\nabla \cdot \mathbf{u} + M\nabla \cdot \mathbf{w}, \quad (6)$$

where ω is the angular frequency, \mathbf{H} is the magnetic field, \mathbf{E} is the electric field, \mathbf{u} is the average solid displacement, \mathbf{w} is the average relative fluid–solid displacement, $\boldsymbol{\tau}$ is the bulk stress tensor, P is the pore fluid pressure, \mathbf{I} is the identity tensor, ϵ and μ are the electrical permittivity and magnetic permeability of the porous formation, respectively. $\rho = (1 - \phi)\rho_s + \phi\rho_f$ is the bulk density, ρ_s is the solid grain density, ρ_f is the pore fluid density, ϕ is the porosity, η is the fluid viscosity. $\sigma(\omega)$, $\kappa(\omega)$ and $L(\omega)$ are the dynamic electrical conductivity, the dynamic permeability and the electrokinetic coupling coefficient, respectively, all of which are complex and frequency dependent. Their detailed expressions can be seen in Pride (1994). \mathbf{F} and \mathbf{f} are the average force densities exerted on the bulk material and fluid phase, respectively. \mathbf{C} and \mathbf{M} are the applied current-density and magnetic-current sources, respectively. H , C and M are the elastic moduli which are expressed as

$$H = K_b + 4G/3 + \alpha^2 M, \quad (7)$$

$$C = \alpha M, \quad (8)$$

$$M = K_f K_s / [\phi K_s + (\alpha - \phi)K_f], \quad (9)$$

where

$$\alpha = 1 - K_b/K_s, \quad (10)$$

K_s and K_f are the bulk moduli of the solid grain and the pore fluid, respectively, K_b and G are the bulk and shear moduli of the framework, respectively.

3 GREEN'S FUNCTIONS FOR POINT SOURCE

The magnetic-current source \mathbf{M} can be excluded because such a term is always due to loops of applied electrical current, which can be represented by a particular distribution of the electrical current \mathbf{C} (Pride & Haartsen 1996). Using the solid displacement \mathbf{u} , the relative fluid–solid displacement \mathbf{w} and the electric field \mathbf{E} as the independent field variables, we rewrite the Pride's equations as

$$[(H - G)\nabla\nabla + (G\nabla^2 + \omega^2\rho)\mathbf{I}] \cdot \mathbf{u} + [C\nabla\nabla + \omega^2\rho_f\mathbf{I}] \cdot \mathbf{w} = -\mathbf{F}, \quad (11)$$

$$[C\nabla\nabla + \omega^2\rho_f\mathbf{I}] \cdot \mathbf{u} + [M\nabla\nabla + \omega^2\tilde{\rho}\mathbf{I}] \cdot \mathbf{w} - i\omega\tilde{\rho}L\mathbf{E} = -\mathbf{f}, \quad (12)$$

$$[\nabla\nabla - (\nabla^2 + \omega^2\mu\tilde{\epsilon})\mathbf{I}] \cdot \mathbf{E} + i\omega^3\mu\tilde{\rho}L\mathbf{w} = i\omega\mu\mathbf{C}, \quad (13)$$

where

$$\tilde{\rho} = i\eta/[\omega\kappa(\omega)], \quad (14)$$

$$\tilde{\epsilon} = \epsilon + i\sigma(\omega)/\omega - \tilde{\rho}L^2(\omega). \quad (15)$$

We consider the source terms in the forms of the Dirac delta function

$$\mathbf{F} = \mathbf{F}_0\delta(\mathbf{r} - \mathbf{r}'), \quad (16)$$

$$\mathbf{f} = \mathbf{f}_0\delta(\mathbf{r} - \mathbf{r}'), \quad (17)$$

$$\mathbf{C} = \mathbf{C}_0\delta(\mathbf{r} - \mathbf{r}'), \quad (18)$$

where $\mathbf{r} = x_i \mathbf{e}_i$ is the position vector of the observation point, $\mathbf{r}' = x'_i \mathbf{e}_i$ is the position vector of the source location, \mathbf{e}_i is the coordinate unit vector, and here the Einstein summation convention for repeated indices is used. The general solutions of eqs (11)–(13) are in following forms

$$\mathbf{u} = \mathbf{G}_u^F \mathbf{F}_0 + \mathbf{G}_u^f \mathbf{f}_0 + \mathbf{G}_u^C \mathbf{C}_0, \quad (19)$$

$$\mathbf{w} = \mathbf{G}_w^F \mathbf{F}_0 + \mathbf{G}_w^f \mathbf{f}_0 + \mathbf{G}_w^C \mathbf{C}_0, \quad (20)$$

$$\mathbf{E} = \mathbf{G}_E^F \mathbf{F}_0 + \mathbf{G}_E^f \mathbf{f}_0 + \mathbf{G}_E^C \mathbf{C}_0, \quad (21)$$

where \mathbf{G}_β^ξ is the Green's function describing the field response of β ($\beta = u, w, E$) type due to the source exerted of ξ ($\xi = F, f, C$) type. By Fourier transforming eqs (11)–(13), and then solving the system of equations, Pride & Haartsen (1996) obtained the Green's functions in the frequency-space domain

$$\begin{aligned} \mathbf{G}_\beta^\xi(\mathbf{r}|\mathbf{r}') = & \sum_{s=s_s}^{s_{em}} T_{\beta,s}^\xi \frac{e^{i\omega s r}}{4\pi r} (\mathbf{I} - \hat{\mathbf{r}}\hat{\mathbf{r}}) + \sum_{s=s_{pf}}^{s_{ps}} L_{\beta,s}^\xi \frac{e^{i\omega s r}}{4\pi r} \hat{\mathbf{r}}\hat{\mathbf{r}} + \left[\sum_{s=s_s}^{s_{em}} T_{\beta,s}^\xi \left(\frac{i}{\omega s r} - \frac{1}{\omega^2 s^2 r^2} \right) \frac{e^{i\omega s r}}{4\pi r} \right. \\ & \left. - \sum_{s=s_{pf}}^{s_{ps}} L_{\beta,s}^\xi \left(\frac{i}{\omega s r} - \frac{1}{\omega^2 s^2 r^2} \right) \frac{e^{i\omega s r}}{4\pi r} \right] (\mathbf{I} - 3\hat{\mathbf{r}}\hat{\mathbf{r}}), \end{aligned} \quad (22)$$

where $r = |\mathbf{r} - \mathbf{r}'|$, and $\hat{\mathbf{r}} = \frac{\mathbf{r} - \mathbf{r}'}{r}$. $\hat{\mathbf{r}} = \hat{r}_i \mathbf{e}_i$ indicates the unit vector pointing from the source location to the observation point. s_{pf} , s_{ps} , s_s and s_{em} are the complex slownesses of the fast P wave (Pf), slow P wave (Ps), shear wave (S) and EM wave, respectively. $T_{\beta,s}^\xi$ and $L_{\beta,s}^\xi$ are the complex amplitudes of the transverse and longitudinal components, respectively. The detailed expressions of the wave slownesses and the complex amplitudes have been derived by Pride & Haartsen (1996). They are listed in Appendix A. The tensorial polarization ($\mathbf{I} - \hat{\mathbf{r}}\hat{\mathbf{r}}$) in expression (22) corresponds to the transverse waves (i.e. the S and EM waves) while $\hat{\mathbf{r}}\hat{\mathbf{r}}$ corresponds to the longitudinal waves (i.e. the Pf and Ps waves). The near field polarization ($\mathbf{I} - 3\hat{\mathbf{r}}\hat{\mathbf{r}}$) can be considered as a combination of the transverse and longitudinal waves.

Pride & Haartsen (1996) did not give the Green's function of the magnetic field. We derive its expression as follows. Ignoring the magnetic-current source in eq. (2), we have

$$\mathbf{H} = \frac{1}{i\omega\mu} \nabla \times \mathbf{E}. \quad (23)$$

Then the Green's function of the magnetic field \mathbf{H} is

$$\mathbf{G}_H^\xi(\mathbf{r}|\mathbf{r}') = \frac{1}{i\omega\mu} \nabla \times \mathbf{G}_E^\xi(\mathbf{r}|\mathbf{r}'). \quad (24)$$

Substituting eq. (22) into eq. (24) with setting the subscript β as E , and noticing the relation

$$\nabla \times \left[-\frac{e^{i\omega s r}}{r} \hat{\mathbf{r}}\hat{\mathbf{r}} + \left(\frac{i}{\omega s r} - \frac{1}{\omega^2 s^2 r^2} \right) \frac{e^{i\omega s r}}{r} (\mathbf{I} - 3\hat{\mathbf{r}}\hat{\mathbf{r}}) \right] = 0, \quad (25)$$

we then have

$$\mathbf{G}_H^\xi(\mathbf{r}|\mathbf{r}') = \frac{1}{i\omega\mu} \sum_{s=s_s}^{s_{em}} T_{E,s}^\xi \frac{e^{i\omega s r}}{4\pi} \left(\frac{i\omega s}{r} - \frac{1}{r^2} \right) \hat{\mathbf{r}} \times \mathbf{I}. \quad (26)$$

The proof of eq. (25) is given in Appendix B. As stated by Pride & Haartsen (1996), only the transverse waves (i.e. the S and EM waves) contribute to the Green's function of the magnetic field while the longitudinal waves (i.e. the Pf and Ps waves) do not. Different from the electric field expressed in eq. (22), the magnetic field due to a single force has only one polarization, that is, $\hat{\mathbf{r}} \times \mathbf{I}$.

To visualize the electric and magnetic fields generated by a single force, we calculate their radiation patterns. The spherical coordinates (Fig. 1) are introduced for the convenience of analysis. In Fig. 1, S denotes the source and is located at the origin, and B denotes the observation point. The cosines \hat{r}_1 , \hat{r}_2 and \hat{r}_3 are defined as follows

$$\hat{r}_1 = \sin \theta \cos \tilde{\phi}, \quad (27a)$$

$$\hat{r}_2 = \sin \theta \sin \tilde{\phi}, \quad (27b)$$

$$\hat{r}_3 = \cos \theta. \quad (27c)$$

Assuming a body force $\mathbf{F} = F_3 \mathbf{e}_3$ is exerted, the electric and magnetic fields are then expressed as

$$\begin{aligned} \mathbf{E} = & \mathbf{G}_E^F(\mathbf{r}|\mathbf{r}') \cdot \mathbf{F} \\ = & \sum_{s=s_s}^{s_{em}} T_{E,s}^F \frac{e^{i\omega s r}}{4\pi r} F \hat{\mathbf{e}}_r^{far} + \sum_{s=s_{pf}}^{s_{ps}} L_{E,s}^F \frac{e^{i\omega s r}}{4\pi r} F \hat{\mathbf{e}}_L^{far} + \left[\sum_{s=s_s}^{s_{em}} T_{E,s}^F \left(\frac{i}{\omega s r} - \frac{1}{\omega^2 s^2 r^2} \right) \frac{e^{i\omega s r}}{4\pi r} \right. \\ & \left. - \sum_{s=s_{pf}}^{s_{ps}} L_{E,s}^F \left(\frac{i}{\omega s r} - \frac{1}{\omega^2 s^2 r^2} \right) \frac{e^{i\omega s r}}{4\pi r} \right] F \hat{\mathbf{e}}^{near}, \end{aligned} \quad (28)$$

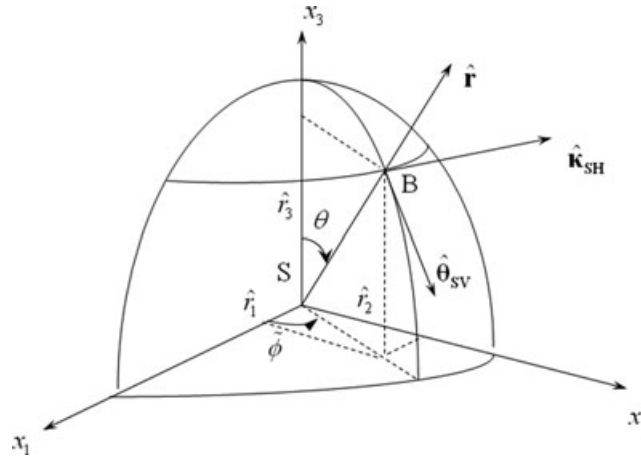


Figure 1. Definition of the cosines \hat{r}_1 , \hat{r}_2 and \hat{r}_3 in spherical coordinates. S indicates the source and is located at the origin. B indicates the observation point. The unit vectors $\hat{\mathbf{r}}$, $\hat{\boldsymbol{\theta}}_{SV}$ and $\hat{\boldsymbol{\kappa}}_{SH}$ are also shown.

and

$$\mathbf{H} = \mathbf{G}_H^F(\mathbf{r}|\mathbf{r}') \cdot \mathbf{F} = \frac{1}{i\omega\mu} \sum_{s=s_S}^{s_{em}} T_{E,s}^F \frac{e^{i\omega s r}}{4\pi} \left(\frac{i\omega s}{r} - \frac{1}{r^2} \right) F \hat{\mathbf{h}}, \quad (29)$$

where

$$\hat{\mathbf{e}}_L^{far} = \hat{r}_3 \hat{\mathbf{r}}, \quad (30a)$$

$$\hat{\mathbf{e}}_T^{far} = \begin{bmatrix} -\hat{r}_1 \hat{r}_3 \\ -\hat{r}_2 \hat{r}_3 \\ 1 - \hat{r}_3 \hat{r}_3 \end{bmatrix}, \quad (30b)$$

$$\hat{\mathbf{e}}^{near} = \begin{bmatrix} -3\hat{r}_1 \hat{r}_3 \\ -3\hat{r}_2 \hat{r}_3 \\ 1 - 3\hat{r}_3 \hat{r}_3 \end{bmatrix}, \quad (30c)$$

$$\hat{\mathbf{h}} = \begin{bmatrix} \hat{r}_2 \\ -\hat{r}_1 \\ 0 \end{bmatrix}. \quad (30d)$$

Expressions (30) show the polarization vectors of the electric and magnetic fields. For the electric field, the far field polarization of longitudinal mode (L mode) $\hat{\mathbf{e}}_L^{far}$ is along the $\hat{\mathbf{r}}$ -direction (i.e. the direction of the wave propagating). The far field of transverse mode (T mode) $\hat{\mathbf{e}}_T^{far}$ can be rewritten as

$$\hat{\mathbf{e}}_T^{far} = -\sin \theta \begin{bmatrix} \cos \theta \cos \tilde{\phi} \\ \cos \theta \sin \tilde{\phi} \\ -\sin \theta \end{bmatrix} = -\sin \theta \hat{\boldsymbol{\theta}}_{SV}. \quad (31)$$

The vector $\hat{\boldsymbol{\theta}}_{SV}$ is shown in Fig. 1. We can easily prove the relation $\hat{\boldsymbol{\theta}}_{SV} \cdot \hat{\mathbf{r}} = 0$, which means that the direction of the electric far field of the transverse wave is orthogonal to the $\hat{\mathbf{r}}$ -direction. The polarization vector of the magnetic field can be rewritten as

$$\hat{\mathbf{h}} = -\sin \theta \begin{bmatrix} -\sin \tilde{\phi} \\ \cos \tilde{\phi} \\ 0 \end{bmatrix} = -\sin \theta \hat{\boldsymbol{\kappa}}_{SH}. \quad (32)$$

The vector $\hat{\boldsymbol{\kappa}}_{SH}$ is also shown in Fig. 1. One can prove the relations $\hat{\boldsymbol{\kappa}}_{SH} \cdot \hat{\mathbf{r}} = 0$ and $\hat{\boldsymbol{\kappa}}_{SH} \cdot \hat{\boldsymbol{\theta}}_{SV} = 0$, respectively. These indicate that the magnetic field is orthogonal to not only the $\hat{\mathbf{r}}$ -direction but also the $\hat{\boldsymbol{\theta}}_{SV}$ -direction. As seen from Fig. 1, $\hat{\boldsymbol{\theta}}_{SV}$ is always along the tangent direction of meridian and is the well-known SV wave polarization vector in elastodynamics, while $\hat{\boldsymbol{\kappa}}_{SH}$ is always along the tangent direction of latitude and is thus the SH wave polarization vector. The third equation of expressions (30) represents the polarization vector of the electric near field, which has following properties:

$$\hat{\mathbf{e}}^{near} \cdot \hat{\mathbf{r}} = -2 \cos \theta, \quad (33a)$$

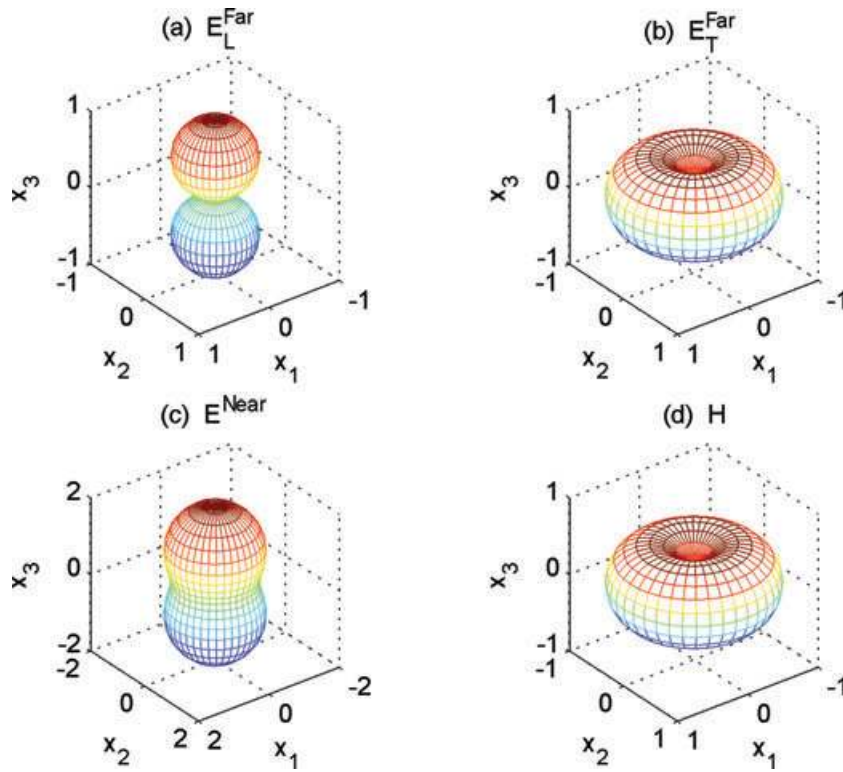


Figure 2. Geometry of 3-D radiation patterns due to a single vertical point force $\mathbf{F} = F_3 \mathbf{e}_3$: (a) electric far field of longitudinal mode, (b) electric far field of transverse mode, (c) electric near field and (d) magnetic field of transverse mode (colour online).

$$\hat{\mathbf{e}}^{\text{near}} \cdot \hat{\boldsymbol{\theta}}_{SV} = -3 \sin \theta \cos \theta, \quad (33b)$$

$$\hat{\mathbf{e}}^{\text{near}} \cdot \hat{\mathbf{r}}_{SH} = 0. \quad (33c)$$

It is implied in eq. (33) that the electric near field radiated by the force $\mathbf{F} = F_3 \mathbf{e}_3$ is parallel to neither the $\hat{\mathbf{r}}$ -direction nor the $\hat{\boldsymbol{\theta}}_{SV}$ -direction. It is, however, in the plane composed of $\hat{\mathbf{r}}$ and $\hat{\boldsymbol{\theta}}_{SV}$, and is orthogonal to the $\hat{\mathbf{r}}_{SH}$ -direction. To get a further understanding, we calculate the radiation patterns of the electric far fields of the L and T modes, as well as the electric near field and the magnetic field. When only considering the amplitudes of the polarization vectors and ignoring all other corresponding constants in eqs (28) and (29), we define

$$E_L^{\text{far}} = |\hat{\mathbf{e}}_L^{\text{far}}| = |\cos \theta|, \quad (34a)$$

$$E_T^{\text{far}} = |\hat{\mathbf{e}}_T^{\text{far}}| = |\sin \theta|, \quad (34b)$$

$$E^{\text{near}} = |\hat{\mathbf{e}}^{\text{near}}| = \sqrt{1 + 3 \cos^2 \theta}, \quad (34c)$$

$$H = |\hat{\mathbf{h}}| = |\sin \theta|. \quad (34d)$$

The radiation pattern of the electric far field of the L mode wave is illustrated in Fig. 2(a), which is similar to that of the far field of an elastic P wave. The radiation pattern of the electric far field of the T mode wave (Fig. 2b) is similar to that of the far field of an elastic S wave. Comparing Fig. 2(b) with Fig. 2(d), we find that for the T mode wave, the electric far field and the magnetic field have the same radiation patterns in geometry, although they differ in the polarizations. Fig. 2(c) shows the radiation pattern of the electric near field, which is quite different from those of the electric far fields of the longitudinal and transverse waves.

4 WAVEFIELDS DUE TO THE MOMENT TENSOR SOURCES

4.1 Moment tensor sources

In seismology, the single point forces are often insufficient to describe real physical sources. For example, an explosive source cannot be represented by a single force. So the moment tensors are usually introduced to model more sources, for example, explosive sources and dislocation type sources (Backus & Mulcahy 1976a,b). In elastodynamics, the displacement due to the moment tensor in the frequency domain is

$$u_i = M_{jk} \frac{\partial G_{u,ij}^F}{\partial r'_k}, \quad (35)$$

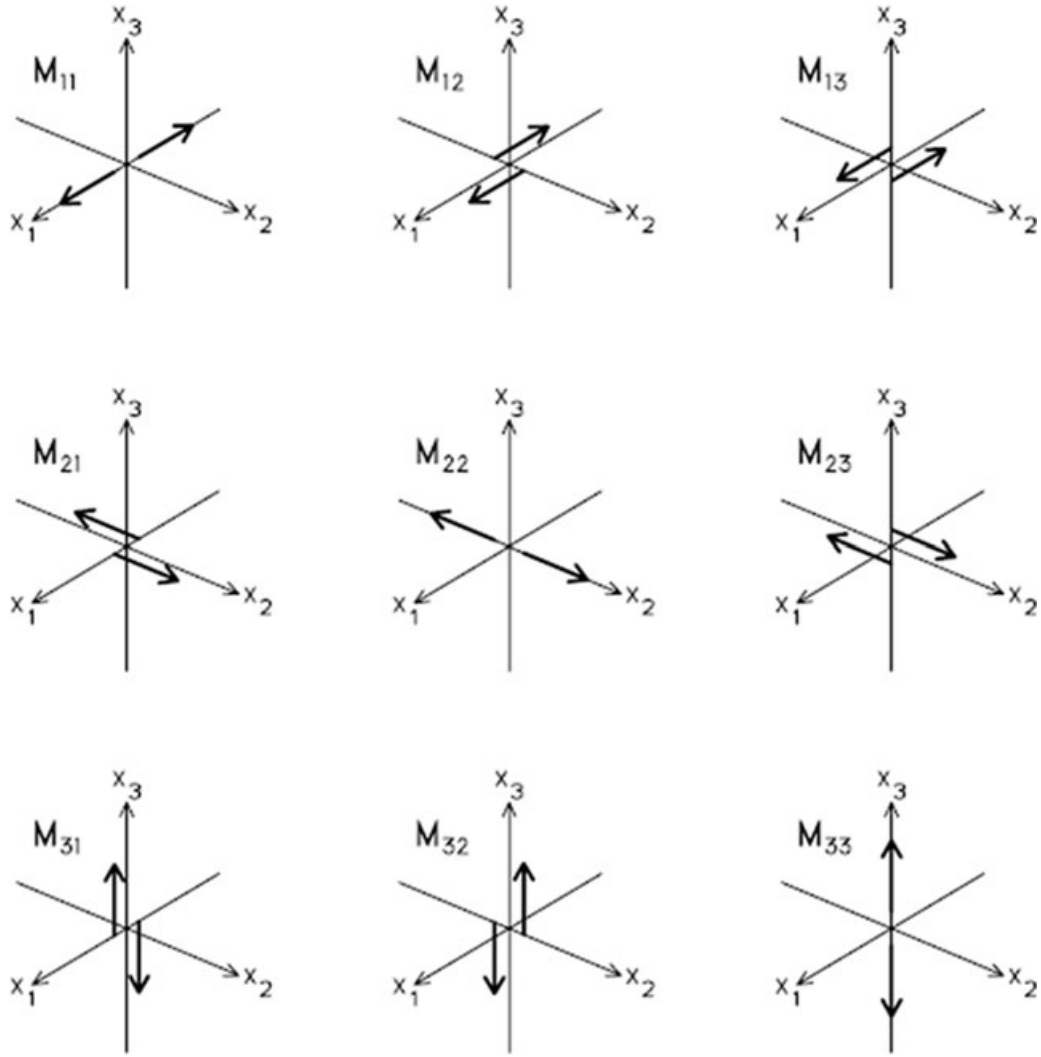


Figure 3. Nine components of moment tensor M_{jk} and their equivalent body force representations. Three of them are dipoles ($j = k$) and the other are couples. For a couple, j and k denote the directions of forces and the arm of the couple, respectively (after Aki & Richards 2002).

where $\mathbf{G}_{u,ij}^F$ is the Green's function of the displacement due to a single force. M_{jk} is the moment tensor component, which is either a dipole when $j = k$ or a couple when $j \neq k$. For a couple, the subscripts j and k denote the directions of the forces and the arm of the couple, respectively. The nine components of the moment tensor are illustrated in Fig. 3 (Aki & Richards 2002).

Eq. (35) is also valid for the solid displacement \mathbf{u} , the relative fluid–solid displacement \mathbf{w} , the electric field \mathbf{E} and the magnetic field \mathbf{H} due to the moment tensors for the coupled poroelastic and EM problem. To obtain the expressions of these fields due to the moment tensors is not difficult since their Green's functions due to a single force have been obtained in the former section. Using eq. (35), after a straightforward but lengthy algebraic manipulation, we get

$$\begin{aligned}
 \beta_i = & \sum_{s=s_s}^{s_{em}} T_{\beta,s}^F \frac{-i\omega s e^{i\omega s r}}{4\pi r} (M_{ij}\hat{r}_j - M_{jk}\hat{r}_i\hat{r}_j\hat{r}_k) + \sum_{s=s_{pf}}^{s_{ps}} L_{\beta,s}^F \frac{-i\omega s e^{i\omega s r}}{4\pi r} (M_{jk}\hat{r}_i\hat{r}_j\hat{r}_k) \\
 & + \sum_{s=s_s}^{s_{em}} T_{\beta,s}^F \frac{e^{i\omega s r}}{4\pi r^2} (M_{jj}\hat{r}_i + M_{ji}\hat{r}_j + 2M_{ij}\hat{r}_j - 6M_{jk}\hat{r}_i\hat{r}_j\hat{r}_k) \\
 & + \sum_{s=s_{pf}}^{s_{ps}} L_{\beta,s}^F \frac{e^{i\omega s r}}{4\pi r^2} (M_{jj}\hat{r}_i + M_{ji}\hat{r}_j + M_{ij}\hat{r}_j - 6M_{jk}\hat{r}_i\hat{r}_j\hat{r}_k) \\
 & + \left[\sum_{s=s_s}^{s_{em}} T_{\beta,s}^F \frac{e^{i\omega s r}}{4\pi} \left(\frac{i}{\omega s r^3} - \frac{1}{\omega^2 s^2 r^4} \right) \right. \\
 & \left. - \sum_{s=s_{pf}}^{s_{ps}} L_{\beta,s}^F \frac{e^{i\omega s r}}{4\pi} \left(\frac{i}{\omega s r^3} - \frac{1}{\omega^2 s^2 r^4} \right) \right] (3M_{jj}\hat{r}_i + 3M_{ji}\hat{r}_j + 3M_{ij}\hat{r}_j - 15M_{jk}\hat{r}_i\hat{r}_j\hat{r}_k),
 \end{aligned} \tag{36}$$

and

$$H_l = \frac{1}{i\omega\mu} \left[\sum_{s=s_g}^{s_{em}} T_{E,s}^F \frac{e^{i\omega sr}}{4\pi} \frac{\omega^2 s^2}{r} M_{jk} \hat{r}_i \hat{r}_k \varepsilon_{ijl} + \sum_{s=s_g}^{s_{em}} T_{E,s}^F \frac{e^{i\omega sr}}{4\pi} \left(-\frac{i\omega s}{r^2} + \frac{1}{r^3} \right) (M_{ji} - 3M_{jk} \hat{r}_i \hat{r}_k) \varepsilon_{ijl} \right], \quad (37)$$

where β can be u, w and E , ε_{ijl} is the permutation symbol. Eq. (36) is similar to the expression of the displacement due to the moment tensors in elastodynamics (Aki & Richards 2002). The β field can be divided into three parts of fields in terms of different geometrical diffusions, namely, the far field with $\frac{1}{r}$ dependency, the intermediate field with $\frac{1}{r^2}$ dependency, and the near field with $(\frac{i}{\omega sr^3} - \frac{1}{\omega^2 s^2 r^4})$ dependency. The magnetic field can also be divided into the far field with $\frac{1}{r}$ dependency and the near field with $(-\frac{i\omega s}{r^2} + \frac{1}{r^3})$ dependency, respectively.

The various combinations of the moment tensor components represent different physical sources. For example, the combination of components $M_{11} + M_{22} + M_{33}$ corresponds to an explosion source, while the combination of components $M_{13} + M_{31}$ corresponds to a double couple source. The double couple is an important source in seismology because it is equivalent to the fault slip, which often causes an earthquake. Many observations suggest that most earthquakes obey the double couple source mechanism (Aki & Richards 2002).

4.2 Electric and magnetic fields due to a double couple

Consider a double couple $M_{13} + M_{31}$, which can represent either a fault in the $x_2 - x_3$ plane with slipping in the x_3 -direction (i.e. a vertical fault) or a fault in the $x_1 - x_2$ plane with slipping in the x_1 -direction (i.e. a horizontal fault). Using eqs (36) and (37), and setting $M_{13} = M_{31} = M_0$, we get the electric field

$$\begin{aligned} \mathbf{E} = & \sum_{s=s_g}^{s_{em}} T_{E,s}^F \frac{-i\omega s e^{i\omega sr}}{4\pi r} M_0 \hat{\mathbf{e}}_T^{far} + \sum_{s=s_{pf}}^{s_{ps}} L_{E,s}^F \frac{-i\omega s e^{i\omega sr}}{4\pi r} M_0 \hat{\mathbf{e}}_L^{far} \\ & + \sum_{s=s_g}^{s_{em}} T_{E,s}^F \frac{e^{i\omega sr}}{4\pi r^2} M_0 \hat{\mathbf{e}}_T^{intermediate} + \sum_{s=s_{pf}}^{s_{ps}} L_{E,s}^F \frac{e^{i\omega sr}}{4\pi r^2} M_0 \hat{\mathbf{e}}_L^{intermediate} \\ & + \left[\sum_{s=s_g}^{s_{em}} T_{E,s}^F \frac{e^{i\omega sr}}{4\pi} \left(\frac{i}{\omega sr^3} - \frac{1}{\omega^2 s^2 r^4} \right) - \sum_{s=s_{pf}}^{s_{ps}} L_{E,s}^F \frac{e^{i\omega sr}}{4\pi} \left(\frac{i}{\omega sr^3} - \frac{1}{\omega^2 s^2 r^4} \right) \right] M_0 \hat{\mathbf{e}}^{near}, \end{aligned} \quad (38)$$

and the magnetic field

$$\mathbf{H} = \frac{1}{i\omega\mu} \left[\sum_{s=s_g}^{s_{em}} T_{E,s}^F \frac{e^{i\omega sr}}{4\pi} \frac{\omega^2 s^2}{r} M_0 \hat{\mathbf{h}}_T^{far} + \sum_{s=s_g}^{s_{em}} T_{E,s}^F \frac{e^{i\omega sr}}{4\pi} \left(-\frac{i\omega s}{r^2} + \frac{1}{r^3} \right) M_0 \hat{\mathbf{h}}_T^{near} \right], \quad (39)$$

where

$$\hat{\mathbf{e}}_T^{far} = \begin{bmatrix} (1 - 2\hat{r}_1^2) \hat{r}_3 \\ -2\hat{r}_1 \hat{r}_2 \hat{r}_3 \\ (1 - 2\hat{r}_3^2) \hat{r}_1 \end{bmatrix}, \quad (40a)$$

$$\hat{\mathbf{e}}_L^{far} = 2\hat{r}_1 \hat{r}_3 \begin{bmatrix} \hat{r}_1 \\ \hat{r}_2 \\ \hat{r}_3 \end{bmatrix}, \quad (40b)$$

$$\hat{\mathbf{e}}_T^{intermediate} = \begin{bmatrix} (3 - 12\hat{r}_1^2) \hat{r}_3 \\ -12\hat{r}_1 \hat{r}_2 \hat{r}_3 \\ (3 - 12\hat{r}_3^2) \hat{r}_1 \end{bmatrix}, \quad (40c)$$

$$\hat{\mathbf{e}}_L^{intermediate} = \begin{bmatrix} (2 - 12\hat{r}_1^2) \hat{r}_3 \\ -12\hat{r}_1 \hat{r}_2 \hat{r}_3 \\ (2 - 12\hat{r}_3^2) \hat{r}_1 \end{bmatrix}, \quad (40d)$$

$$\hat{\mathbf{e}}^{near} = \begin{bmatrix} (6 - 30\hat{r}_1^2) \hat{r}_3 \\ -30\hat{r}_1 \hat{r}_2 \hat{r}_3 \\ (6 - 30\hat{r}_3^2) \hat{r}_1 \end{bmatrix}, \quad (40e)$$

$$\hat{\mathbf{h}}_T^{far} = \begin{bmatrix} \hat{r}_1 \hat{r}_2 \\ \hat{r}_3^2 - \hat{r}_1^2 \\ -\hat{r}_2 \hat{r}_3 \end{bmatrix}, \quad (40f)$$

$$\hat{\mathbf{h}}_T^{\text{near}} = -3 \begin{bmatrix} \hat{r}_1 \hat{r}_2 \\ (\hat{r}_3^2 - \hat{r}_1^2) \\ -\hat{r}_2 \hat{r}_3 \end{bmatrix}. \quad (40g)$$

The first two equations of expressions (40) denote the polarization vectors of the electric far fields of the L and T mode waves, respectively, and the following two terms represent the polarization vectors of the electric intermediate fields of the L and T mode waves, respectively. The fifth term corresponds to the electric near field. The last two terms denote the magnetic far field and near field. One can get the expressions of the solid displacement \mathbf{u} simply by changing $T_{E,s}^F$ to $T_{u,s}^F$ and $L_{E,s}^F$ to $L_{u,s}^F$, or the relative fluid–solid displacement \mathbf{w} by changing $T_{E,s}^F$ to $T_{w,s}^F$ and $L_{E,s}^F$ to $L_{w,s}^F$ in eq. (38). However, in this paper we aim to investigate the characteristics of the electric and magnetic fields, and thus we do not expand on the seismic fields in the following sections.

4.2.1 Far field

We can rewrite the second equation of expressions (40) as

$$\hat{\mathbf{e}}_L^{\text{far}} = \sin 2\theta \cos \tilde{\phi} \hat{\mathbf{r}}, \quad (41)$$

which indicates the electric far field of L mode is along the $\hat{\mathbf{r}}$ -direction. It is easy to validate the following relation:

$$\hat{\mathbf{e}}_T^{\text{far}} \cdot \hat{\mathbf{r}} = 0. \quad (42)$$

Eq. (42) reveals that the electric far field polarization of transverse mode is perpendicular to the $\hat{\mathbf{r}}$ -direction. In elastodynamics, the transverse waves can be decomposed into two types of waves in light of their alternative polarizations, namely, the SV wave with $\hat{\boldsymbol{\theta}}_{SV}$ polarization and the SH wave with $\hat{\mathbf{k}}_{SH}$ polarization. Similarly, in this paper, when projecting $\hat{\mathbf{e}}_T^{\text{far}}$ to $\hat{\boldsymbol{\theta}}_{SV}$ and $\hat{\mathbf{k}}_{SH}$, respectively, we get

$$\hat{\mathbf{e}}_{SV}^{\text{far}} = (\hat{\mathbf{e}}_T^{\text{far}} \cdot \hat{\boldsymbol{\theta}}_{SV}) \hat{\boldsymbol{\theta}}_{SV} = \cos 2\theta \cos \tilde{\phi} \hat{\boldsymbol{\theta}}_{SV}, \quad (43a)$$

$$\hat{\mathbf{e}}_{SH}^{\text{far}} = (\hat{\mathbf{e}}_T^{\text{far}} \cdot \hat{\mathbf{k}}_{SH}) \hat{\mathbf{k}}_{SH} = -\cos \theta \sin \tilde{\phi} \hat{\mathbf{k}}_{SH}. \quad (43b)$$

It is shown that the electric far field of the T mode wave could also be decomposed into those of SV and SH modes, respectively. We can also prove the validity of the relations below

$$\hat{\mathbf{h}}_T^{\text{far}} \cdot \hat{\mathbf{r}} = 0, \quad (44a)$$

$$\hat{\mathbf{h}}_T^{\text{far}} \cdot \hat{\mathbf{e}}_T^{\text{far}} = 0. \quad (44b)$$

Eqs (44a) and (44b) imply that the magnetic far field is perpendicular to not only the $\hat{\mathbf{r}}$ -direction but also the $\hat{\mathbf{e}}_T^{\text{far}}$ -direction. As those three unit vectors $\hat{\mathbf{r}}$, $\hat{\boldsymbol{\theta}}_{SV}$ and $\hat{\mathbf{k}}_{SH}$ are pairwise orthogonal, we deduce that an SV mode wave with an electric far field in the $\hat{\boldsymbol{\theta}}_{SV}$ -direction should have a magnetic far field in the $\hat{\mathbf{k}}_{SH}$ -direction, while an SH mode wave with an electric far field in the $\hat{\mathbf{k}}_{SH}$ -direction should own a magnetic far field in the $\hat{\boldsymbol{\theta}}_{SV}$ -direction. As a result, we have

$$\hat{\mathbf{h}}_{SV}^{\text{far}} = (\hat{\mathbf{h}}_T^{\text{far}} \cdot \hat{\mathbf{k}}_{SH}) \hat{\mathbf{k}}_{SH} = \cos 2\theta \cos \tilde{\phi} \hat{\mathbf{k}}_{SH}, \quad (45a)$$

$$\hat{\mathbf{h}}_{SH}^{\text{far}} = (\hat{\mathbf{h}}_T^{\text{far}} \cdot \hat{\boldsymbol{\theta}}_{SV}) \hat{\boldsymbol{\theta}}_{SV} = \cos \theta \sin \tilde{\phi} \hat{\boldsymbol{\theta}}_{SV}. \quad (45b)$$

An EM wave of SV mode is also called a TM wave due to the horizontality of the magnetic field, while an EM wave of SH mode is called a TE wave due to the horizontality of the electric field. From the expressions (41), (43) and (45), we calculate the amplitudes of the polarization vectors of the electric far fields for the L mode waves

$$E_L^{\text{far}} = |\hat{\mathbf{e}}_L^{\text{far}}| = |\sin 2\theta \cos \tilde{\phi}|, \quad (46)$$

and for the SV and SH mode waves

$$E_{SV}^{\text{far}} = |\hat{\mathbf{e}}_{SV}^{\text{far}}| = |\cos 2\theta \cos \tilde{\phi}|, \quad (47a)$$

$$E_{SH}^{\text{far}} = |\hat{\mathbf{e}}_{SH}^{\text{far}}| = |\cos \theta \sin \tilde{\phi}|. \quad (47b)$$

The amplitudes of the polarization vectors of the magnetic far fields for the SV and SH mode waves are

$$H_{SV}^{\text{far}} = |\hat{\mathbf{h}}_{SV}^{\text{far}}| = |\cos 2\theta \cos \tilde{\phi}|, \quad (48a)$$

$$H_{SH}^{\text{far}} = |\hat{\mathbf{h}}_{SH}^{\text{far}}| = |\cos \theta \sin \tilde{\phi}|. \quad (48b)$$

The amplitude of the polarization vector of the electric far field for the whole T mode wave is

$$E_T^{\text{far}} = \sqrt{(E_{SV}^{\text{far}})^2 + (E_{SH}^{\text{far}})^2} = \sqrt{\cos^2 2\theta \cos^2 \tilde{\phi} + \cos^2 \theta \sin^2 \tilde{\phi}}. \quad (49)$$

The amplitude of the polarization vector of the magnetic far field for the whole T mode wave is

$$H_T^{\text{far}} = \sqrt{(H_{SV}^{\text{far}})^2 + (H_{SH}^{\text{far}})^2} = \sqrt{\cos^2 2\theta \cos^2 \tilde{\phi} + \cos^2 \theta \sin^2 \tilde{\phi}}. \quad (50)$$

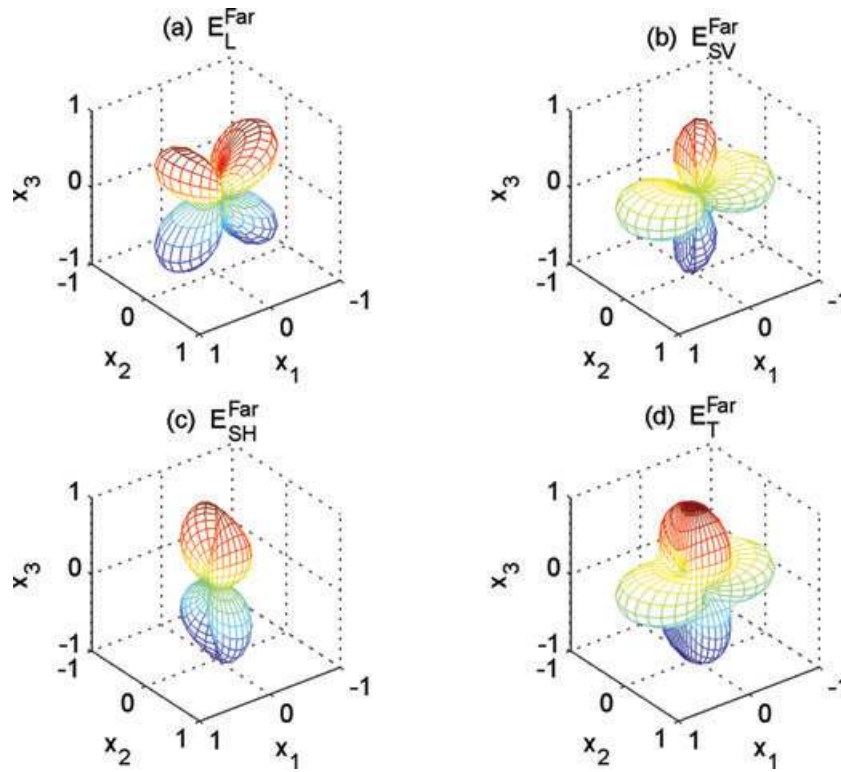


Figure 4. Geometry of 3-D radiation patterns due to a double couple source $M_{13} + M_{31}$: (a) electric far field of the L mode wave, (b) electric far field of the SV mode wave, (c) electric far field of the SH mode wave and (d) electric far field of the T mode wave (colour online).

Using eqs (46)–(50) we plot the radiation patterns for these fields in Fig. 4. Fig. 4(a) shows the radiation pattern of the electric far field of the L mode wave is like a four-leaved clover. It is the same in geometry as that of the P wave in elastodynamics (Aki & Richards 2002). As seen in Figs 4(b)–(d), the radiation patterns of the electric far fields of the SV , SH and whole T mode waves are similar in shape to those of the SV , SH and S waves in elastodynamics, respectively (Aki & Richards 2002; Pujol 2003). Comparing Fig. 4(b) with Fig. 5(a), we find that the electric far field and magnetic far field for the SV mode wave have the radiation patterns although they differ in polarizations. Similar conclusions can be obtained for the SH mode wave and the whole T mode wave by comparing Fig. 4(c) with Fig. 5(b) and Fig. 4(d) with Fig. 5(c), respectively.

4.2.2 Near field

In seismology, usually we only consider the far-field terms of the seismic waves radiated by the seismic source at a long distance away from the source, where the near-field terms hardly contribute to the total wavefield and can be ignored. For the coupled poroelastic and EM case, the wavelength of an EM wave is always much larger than that of a seismic wave (P or S wave) at the same frequency. There possibly exists an observation point, where for the seismic wave the far-field term dominates the total field while for the EM wave the near-field term dominates the total field. In this situation, the near-field term of the EM wave cannot be ignored any longer, and should be taken into account. From eqs (38), the geometrical diffusions of the far-field term, the intermediate-field term and the near-field term of the body waves are denoted as

$$D_{\alpha}^{\text{far}} = \frac{-i\omega s_{\alpha}}{r}, \quad (51a)$$

$$D_{\alpha}^{\text{intermediate}} = \frac{1}{r^2}, \quad (51b)$$

$$D_{\alpha}^{\text{near}} = \left(\frac{i}{\omega s_{\alpha} r^3} - \frac{1}{\omega^2 s_{\alpha}^2 r^4} \right), \quad \alpha = pf, ps, s, em. \quad (51c)$$

Using expressions (51) and ignoring the other constants in eq. (38), the absolute values of the far, intermediate and near fields versus receiver-to-source distance r for each wave are calculated (Fig. 6). The parameters are specified in Table 1 and the frequency is chosen as 1 Hz. As seen from Fig. 6(a), for the Pf wave the absolute value of the far-field term is larger than those of the intermediate- and near-field terms when $r \geq 0.8$ km. For the S wave the far-field term is dominant when $r \geq 0.5$ km (Fig. 6c). For the Ps wave the far-field term is always dominant when $r > 100$ m (Fig. 6d). However, the dividing point between the far-field-dominating and near-field-dominating domains for the EM wave is about 25 km. When the frequency is decreased to 0.1 Hz (the other parameters is kept), we find the dividing point for the EM wave increases to about 60 km (Fig. 7a); When the salinity is decreased to 0.0001 mol/L (the other parameters is kept and the frequency is

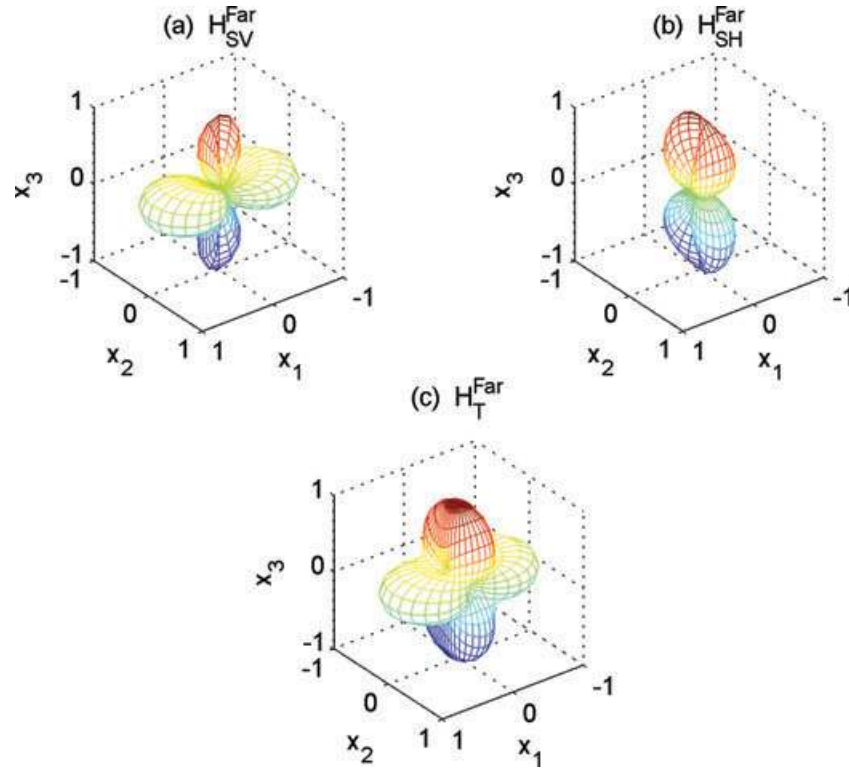


Figure 5. Geometry of 3-D radiation patterns due to a double couple source $M_{13} + M_{31}$: (a) magnetic far field of the *SV* mode wave, (b) magnetic far field of the *SH* mode wave and (c) magnetic far field of the *T* mode wave (colour online).

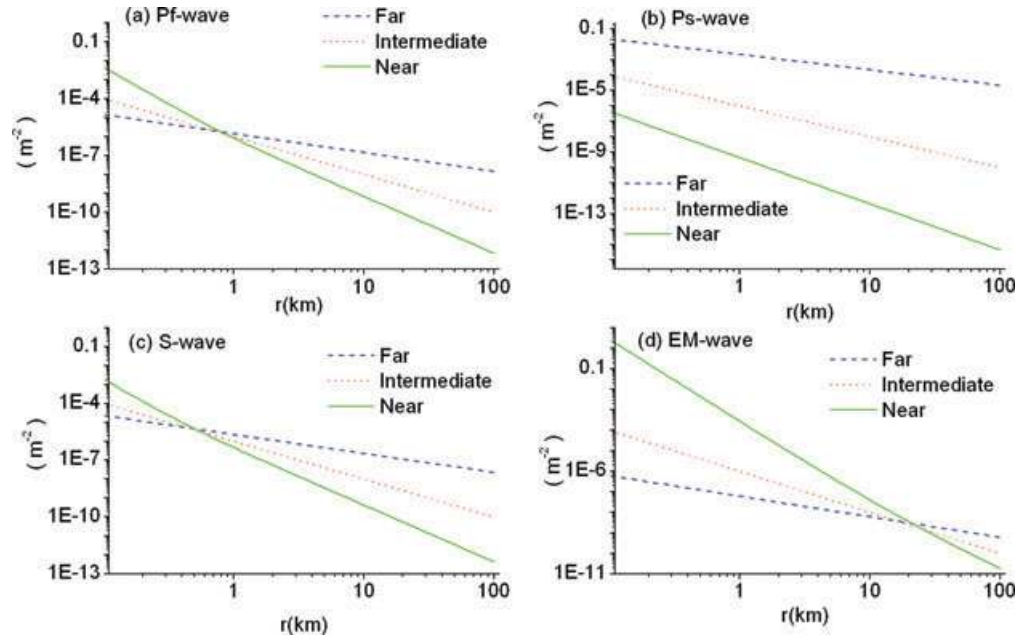


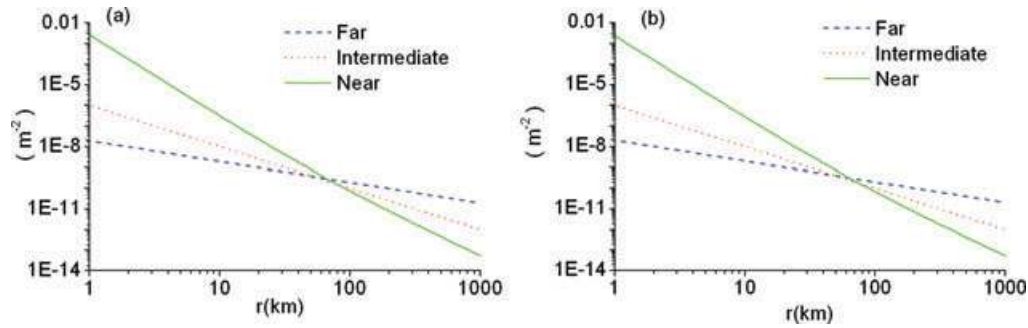
Figure 6. Comparison among the far field (dash line), the intermediate field (dotted line) and the near field (solid line) for (a) *Pf* wave, (b) *Ps* wave, (c) *S* wave and (d) *EM* wave when $f = 1$ Hz and $C_0 = 0.001$ mol L^{-1} (colour online).

1 Hz), such a dividing point increases to about 70 km (Fig. 7b). This means that for the *EM* wave the near-field term has a large dominating distance. Such a dominating distance is sensitive to the frequency and the salinity. Another phenomenon should be noticed is that for each of the body waves the intermediate-field term is never dominant whatever the receiver-to-source distance is chosen (Aki & Richards 2002). For this reason, we leave this kind of field out of discussion. From eq. (38) we know that the electric near field is a combination of all the four body waves, of which the polarization is \hat{e}^{near} . It is not difficult to obtain the following relations:

$$\hat{e}^{\text{near}} \cdot \hat{r} = -18\hat{r}_1\hat{r}_3, \quad (52a)$$

Table 1. Parameters of the porous medium used for the calculation.

Porosity	$\phi = 0.15$
Permeability	$\kappa_0 = 0.1$ mD
Tortuosity	$\alpha_\infty = 3$
Solid grain bulk modulus	$K_s = 35.7$ GPa
Frame bulk modulus	$K_b = 17.91$ GPa
Shear modulus	$G = 17.79$ GPa
Fluid bulk modulus	$K_f = 2.25$ GPa
Solid grain density	$\rho_s = 2650$ kg m ⁻³
Fluid density	$\rho_f = 1000$ kg m ⁻³
Fluid viscosity	$\eta = 0.001$ Pas
Salinity	$C_0 = 0.001$ mol L ⁻¹
Solid relative permittivity	$\varepsilon_s = 4$
Fluid relative permittivity	$\varepsilon_f = 80$
Velocity of <i>P</i> wave	$V_P = 4322$ m s ⁻¹
Velocity of <i>S</i> wave	$V_S = 2721$ m s ⁻¹

**Figure 7.** Comparison among the far field (dash line), the intermediate field (dot line) and the near field (solid line) for *EM* wave when (a) $f = 0.1$ Hz, $C_0 = 0.001$ mol L⁻¹, (b) $f = 1$ Hz, $C_0 = 0.0001$ mol L⁻¹ (colour online).

$$\hat{\mathbf{e}}^{\text{near}} \times \hat{\mathbf{r}} = 6 \left[-\hat{r}_1 \hat{r}_2, \hat{r}_1^2 - \hat{r}_3^2, \hat{r}_2 \hat{r}_3 \right]^T = -6 \hat{\mathbf{h}}_T^{\text{far}}, \quad (52b)$$

$$\hat{\mathbf{e}}^{\text{near}} \cdot \hat{\mathbf{h}}_T^{\text{far}} = 0. \quad (52c)$$

It is implied that the electric near field is neither parallel nor perpendicular to the $\hat{\mathbf{r}}$ -direction, but is perpendicular to the $\hat{\mathbf{h}}_T^{\text{far}}$ -direction. From eqs (40f) and (40g), we find the direction of the magnetic near field is parallel and opposite to the magnetic far field. Using the fifth and seventh equations of expressions (40), we calculate the amplitudes of the electric and magnetic near fields

$$E^{\text{near}} = |\hat{\mathbf{e}}^{\text{near}}| = 6 \sqrt{\sin^2 \theta \cos^2 \tilde{\phi} + \cos^2 \theta + 5 \sin^2 \theta \cos^2 \theta \cos^2 \tilde{\phi}}, \quad (53)$$

$$H^{\text{near}} = |\hat{\mathbf{h}}^{\text{near}}| = 3 \sqrt{\cos^2 2\theta \cos^2 \tilde{\phi} + \cos^2 \theta \sin^2 \tilde{\phi}}, \quad (54)$$

and plot their radiation patterns in Fig. 8. Comparing Fig. 8(a) with Fig. 4, we find the radiation pattern of the electric near field is the same as neither that of the electric far field of L mode nor that of the electric far field of T mode. Comparing Fig. 8(b) with Fig. 5(c), we find that the radiation pattern of the magnetic near field shares the same shape with that of the magnetic far field. The 2-D radiation patterns of the electric and magnetic near fields in the $x_1 - x_3$ plane are exhibited to help us get a further understanding (Fig. 9).

4.2.3 Waveforms in the time domain

The Green's functions expressed in eqs (38) and (39) are presented in the frequency-space domain. Due to the Darcy viscous dissipation, we are not able to analytically transform these Green's functions back into the time domain. However, the numerical time responses can be obtained by the discrete Fourier transform on these Green's functions.

Consider a simple geological model, that is, a uniform infinite porous medium. The parameters of the porous medium are listed in Table 1. The coordinates are illustrated as in Fig. 1. A double couple source $M_{13} + M_{31}$ is located at the origin, and the location of the observation point B is ($x_1 = 60$ km, $x_2 = 1$ km, $x_3 = 15$ km). The moment is chosen as $M_{13} = M_{31} = M_0 = 4.37 \times 10^{17}$ Nm, which corresponds to a M_w 5.7 earthquake. The source used in this paper is a pulse source with a finite frequency band. The time function is

$$s_0(t) = \begin{cases} \frac{1}{2} \left[1 + \cos \frac{2\pi}{T_c} \left(t - \frac{T_c}{2} \right) \right] \cos 2\pi f_0 \left(t - \frac{T_c}{2} \right), & 0 \leq t \leq T \\ 0, & t < 0 \text{ or } t > T_c, \end{cases} \quad (55)$$

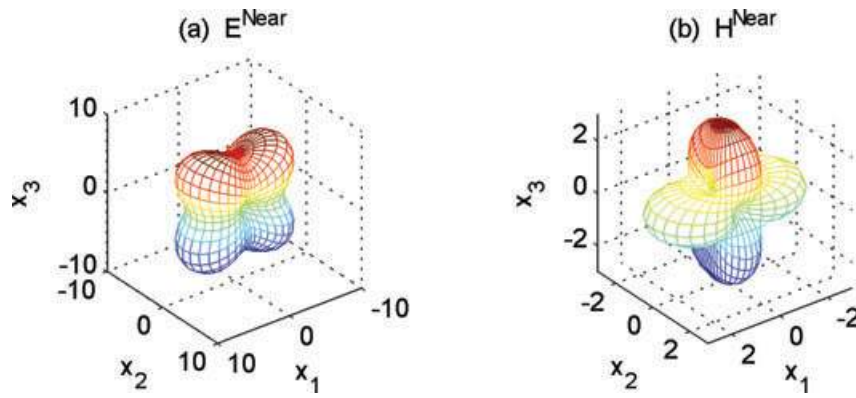


Figure 8. Geometry of 3-D radiation patterns for (a) electric near field (b) magnetic near field due to a double couple source $M_{13} + M_{31}$ (colour online).

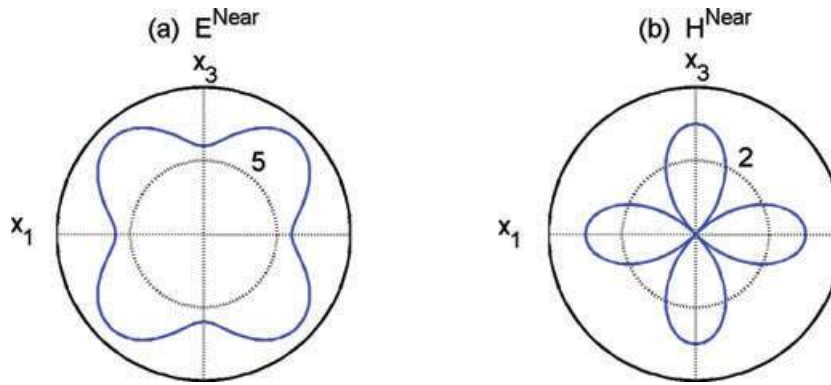


Figure 9. 2-D radiation patterns for (a) electric near field, (b) magnetic near field in $x_1 - x_3$ plane due to a double couple source $M_{13} + M_{31}$ (colour online).

where f_0 and T_c denote the centre frequency and the width of the pulse, respectively. In this paper, we choose $f_0 = 1$ Hz and $T_c = 2.2$ s in the calculation. The frequency varies in the range 0.1–1.9 Hz. Let $s_0(\omega)$ be the frequency response of $s_0(t)$. By changing $T_{E,s}^F$ to $T_{u,s}^F$ and $L_{E,s}^F$ to $L_{u,s}^F$ in eqs (38), we can get the expression of the solid displacement \mathbf{u} . Multiplying both eqs (38) and (39) by $s_0(\omega)$, respectively, and Fourier-transforming them into the time domain, we get the waveforms of the solid displacement, the electric and magnetic fields at observation point B (Figs 10–12, dotted lines). The distance from S to B is about $r = 62$ km. At about $t = 14$ s the P wave arrives, followed by the S wave arriving at $t = 22$ s (Fig. 10). As can be seen from Fig. 11, there is an electric disturbance beginning at the arrival time of the P wave. This is the so-called accompanying electric field induced by the P wave as local material response (Haartsen & Pride 1997). From eq. (38), we know that the S wave can also induce electric field. But such an electric field is too weak to be apparent compared with the P -wave-inducing electric field. It can be seen in the waveform of E_3 (Fig. 11c), although not clearly. We theoretically prove that the S wave usually has a weaker electric-field-inducing ability than the P wave. The proof is in Appendix C. There is a magnetic field disturbance (Fig. 12) beginning at the arrival time of the S wave. Such a magnetic field is induced by the S wave, and is thus an accompanying magnetic field. In both Fig. 11 and Fig. 12, there are electric and magnetic disturbances, which come into view immediately after the source launched. This is the EM wave. It has been amplified by a factor 10 000 in order to be apparent. As its velocity is at least one magnitude larger than the seismic waves (see Table 2), it almost takes no time to reach the observation point. As predicted in eq. (39), only the transverse waves can cause magnetic fields, so we observe no magnetic field accompanying the P wave. Although the P_s wave is predicted in eq. (38), it does not appear in the waveforms of \mathbf{u} or \mathbf{E} due to its strong attenuation.

We have obtained the waveforms in the space-time domain through above process. In this paper, we name this Green's-function method. To validate these waveforms as well as eqs (38) and (39), another method is introduced to calculate the waveforms at point B. The main idea of such a method is regarding the source as a displacement–stress–EM discontinuity vector on the horizontal plane at the source depth. The effect of the point source is represented by the body force terms in eqs (1)–(4). The related formulas have been shown in detail by Haartsen & Pride (1997), Garambois & Dietrich (2002), and also White & Zhou (2006). However, few authors have considered the double couple source. In order to calculate the wavefields induced by the double couple source, we have to derive the corresponding displacement–stress–EM discontinuity vector. The derivation is somewhat lengthy, and is given in Appendix D. To distinguish from the Green's function method (take G-method for short) above, we name the latter equivalent-body-force method (take E-method for short). Using the E-method, the waveforms of \mathbf{u} , \mathbf{E} and \mathbf{H} at point B are calculated, and plotted again in Figs 10–12 (solid lines). As expected, the waveforms from the two methods show an excellent agreement.

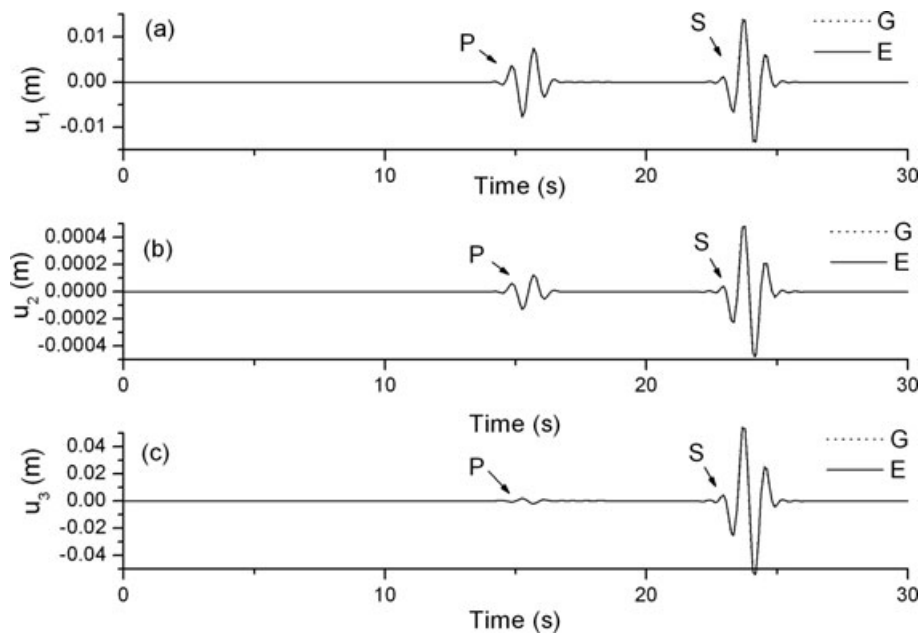


Figure 10. Waveforms of the solid displacement \mathbf{u} at point B. 'G' (dotted line) corresponds to the Green's function method while 'E' (solid line) corresponds to the equivalent-body-force method.

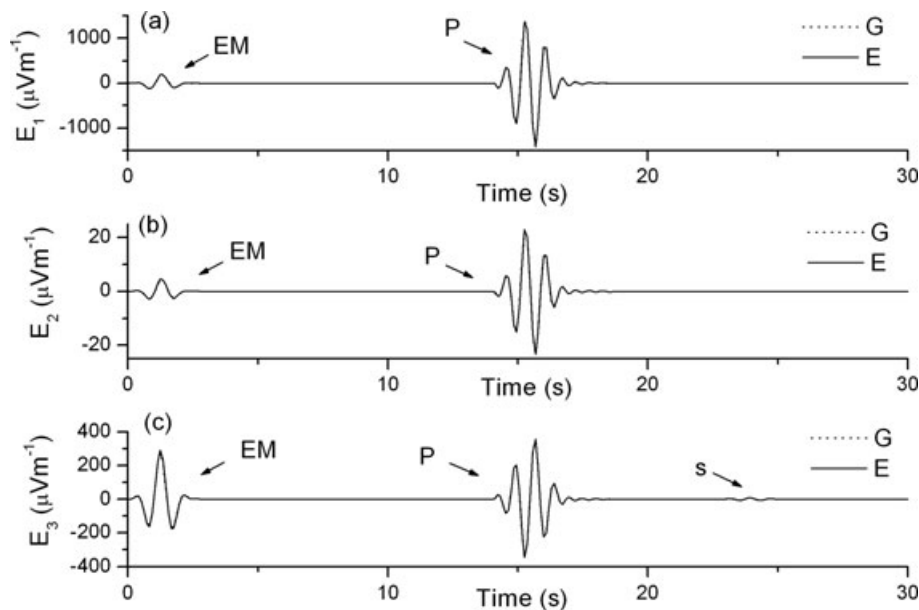


Figure 11. Waveforms of the electric field \mathbf{E} at point B. 'G' (dotted line) corresponds to the Green's function method while 'E' (solid line) corresponds to the equivalent-body-force method. The EM wave has been amplified by a factor 10 000 in order to be apparent.

4.2.4 Influence of observation orientation on the observed waveforms

Pride & Haartsen (1996) have shown that the solid displacement vector \mathbf{u} and the electric field vector \mathbf{E} are always in the same direction, and one can get the expressions of \mathbf{u} by simply changing $T_{E,s}^F$ to $T_{u,s}^F$ and $L_{E,s}^F$ to $L_{u,s}^F$ in eq. (38). For each of the body waves, the far-, intermediate- and near-field terms of the solid displacement must have the same polarization vectors as the corresponding terms of the electric field. This means that the solid displacement must have the same radiation patterns as the electric field. From the radiation patterns (Figs. 2, 4, 5, 8 and 9), we know that the electric and magnetic fields have different amplitudes in different directions. In order to illustrate this phenomenon and to get a further understanding of the radiation patterns, we investigate the waveforms at some special observation points in this section.

We consider an observation point C, which is located on the x_3 -axis in the x_1 - x_3 -plane (Fig. 13). In Fig. 13, the dashed and solid lines represent the 2-D-radiation patterns of the electric field (or the solid displacement) of the longitudinal and transverse waves, respectively. The distance from the source S to the point C is the same to that from S to B, that is, $r = 62$ km. At point C, we have $\theta = 0$ and $\phi = 0$. So we

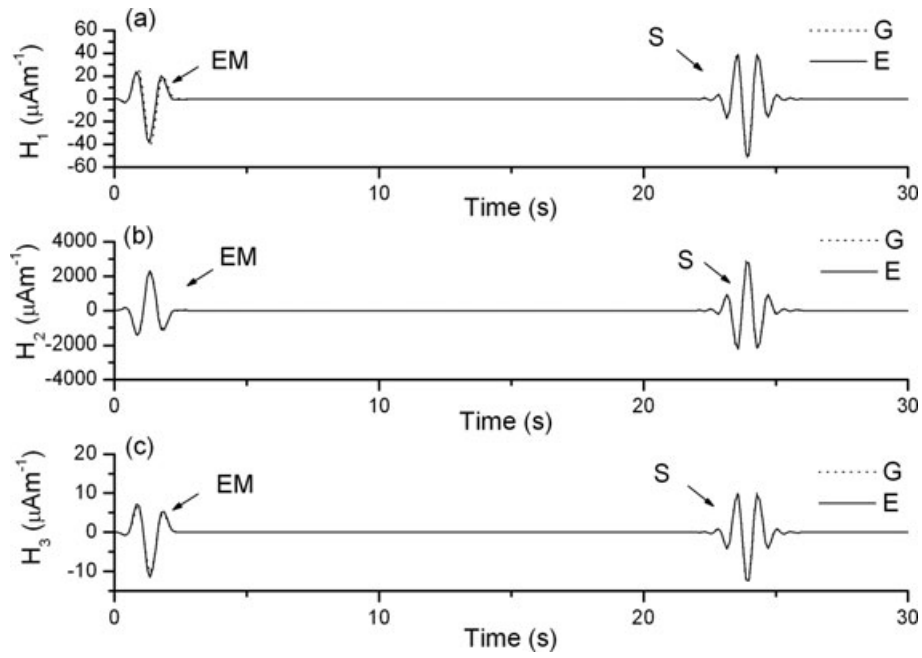


Figure 12. Waveforms of the magnetic field \mathbf{H} at point B. ‘G’ (dotted line) corresponds to the Green’s function method while ‘E’ (solid line) corresponds to the equivalent-body-force method. The *EM* wave has been amplified by a factor 10 000 in order to be apparent.

Table 2. Velocities of the four body waves of the porous medium at $f = 0.1$ Hz and $f = 1.9$ Hz.

Property	Frequency	
	$f = 0.1$ Hz	$f = 1.9$ Hz
<i>Pf</i> -wave velocity (m s^{-1})	4322–0.00002i	4322–0.0004i
<i>Ps</i> -wave velocity (m s^{-1})	0.6174–0.6174i	2.7613–2.7612i
<i>S</i> -wave velocity (m s^{-1})	2721.3–0.00003i	2721.3–0.0007i
<i>EM</i> -wave velocity (m s^{-1})	23005–23005i	102880–102880i

obtain $\hat{r}_1 = 0$, $\hat{r}_2 = 0$ and $\hat{r}_3 = 1$ according to expressions (27). Using expressions (40), we have

$$\hat{\mathbf{e}}_T^{\text{far}} = \begin{bmatrix} 1 \\ 0 \\ 0 \end{bmatrix}, \quad (56a)$$

$$\hat{\mathbf{e}}_L^{\text{far}} = \begin{bmatrix} 0 \\ 0 \\ 0 \end{bmatrix}, \quad (56b)$$

$$\hat{\mathbf{e}}_T^{\text{intermediate}} = \begin{bmatrix} 3 \\ 0 \\ 0 \end{bmatrix}, \quad (56c)$$

$$\hat{\mathbf{e}}_L^{\text{intermediate}} = \begin{bmatrix} 2 \\ 0 \\ 0 \end{bmatrix}, \quad (56d)$$

$$\hat{\mathbf{e}}^{\text{near}} = \begin{bmatrix} 6 \\ 0 \\ 0 \end{bmatrix}, \quad (56e)$$

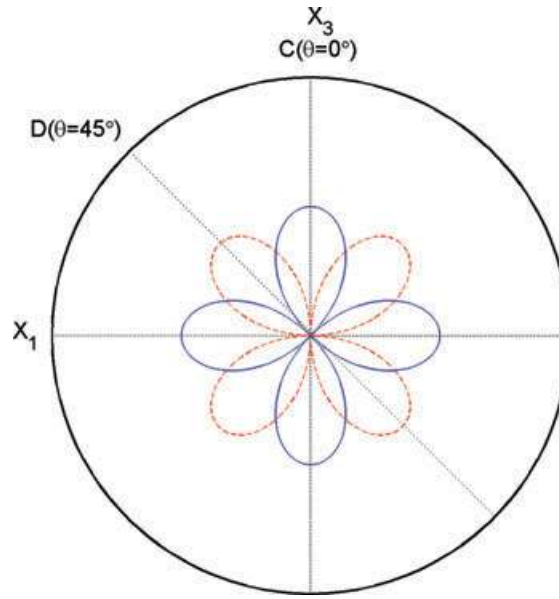


Figure 13. Locations of the observation points C ($\theta = 0^\circ$) and D ($\theta = 45^\circ$) in the $x_1 - x_3$ plane (colour online). The dashed and solid lines represent the 2-D-radiation patterns of the far field of the electric field (or the solid displacement) for the longitudinal and transverse waves, respectively.

$$\mathbf{h}_T^{\text{far}} = \begin{bmatrix} 0 \\ 1 \\ 0 \end{bmatrix}, \quad (56f)$$

$$\mathbf{h}_T^{\text{near}} = \begin{bmatrix} 0 \\ -3 \\ 0 \end{bmatrix}. \quad (56g)$$

According to expressions 56, only the x_1 -component of the electric field (or the solid displacement) and the x_2 -component of the magnetic field are non-zero. So only the waveforms of u_1 , E_1 and H_2 are considered and plotted (Fig. 14). In Fig. 14(a), only the S wave that arrives at $t = 22$ s can be seen, whereas the P wave signal that should appear at $t = 14$ s cannot be seen. The reasons are as follows: (1) as shown in eq. (56b), the far field of the P wave is zero; (2) meanwhile, as illustrated in Figs. 6(a) and (c), both the P and S waves are far-field-dominating at $r = 62$ km, and in addition, both the intermediate and near fields of the P wave are much smaller than the far field of the S wave at $r = 62$ km. Although the P -wave signal is not apparent in the displacement gram (Fig. 14a), the electric field accompanying

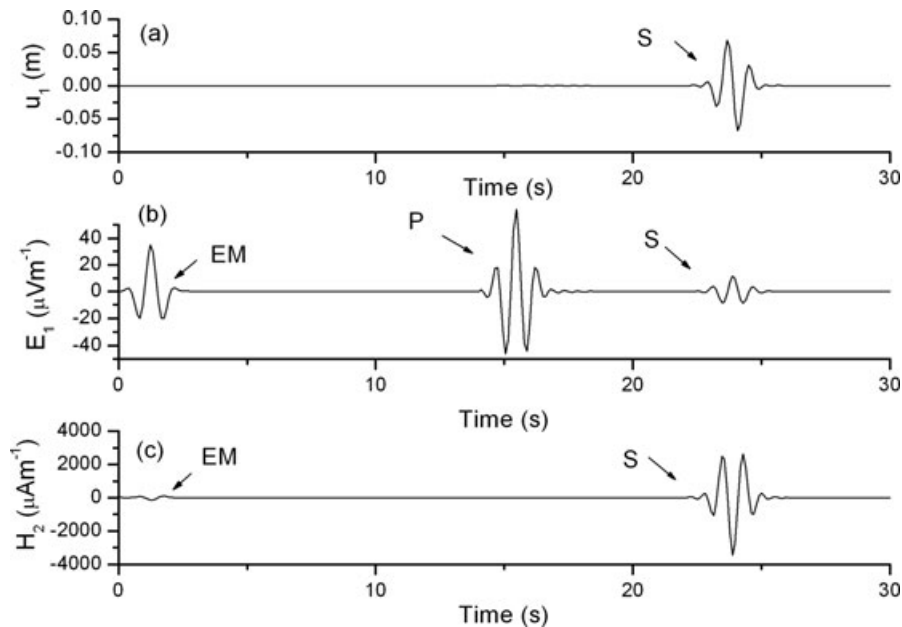


Figure 14. Waveforms of u_1 , E_1 and H_2 at point C . The EM wave has been amplified by a factor 1000 in order to be apparent.

the P wave, which arrives at $t = 14$ s is prominent in the electric field gram (Fig. 14b), and is even stronger than that accompanying the S wave, which arrives at $t = 22$ s. This is because the intermediate and near fields of the P wave are non-zero, and the P wave has a stronger electric-field-inducing ability than the S wave. The intermediate and near fields of the P wave play an important role in inducing electric field at this observation point. However, by comparing Fig. 11(a) with Fig. 14(b), we find that the electric field accompanying the P wave recorded at point C is much weaker than that recorded at point B. The maximum amplitude of the former is about $1400 \mu\text{V m}^{-1}$, while that of the latter is about $46 \mu\text{V m}^{-1}$. In Fig. 14(c) we can see the magnetic field signal induced by the S wave. There are also electric and magnetic field disturbances due to the EM wave in the electric and magnetic field grams (Figs 14b and c). Both of them have been amplified by a factor of 1000.

Consider another observation point D, which is also located in the x_1 – x_3 plane (Fig. 13) with $\theta = 45^\circ$ and $\tilde{\phi} = 0$. The observation-source distance is still chosen as $r = 62$ km. We have $\hat{r}_1 = \sqrt{2}/2$, $\hat{r}_2 = 0$ and $\hat{r}_3 = \sqrt{2}/2$ according to expressions (27). Using expressions (40), we then have

$$\hat{\mathbf{e}}_T^{\text{far}} = \begin{bmatrix} 0 \\ 0 \\ 0 \end{bmatrix}, \quad (57a)$$

$$\hat{\mathbf{e}}_L^{\text{far}} = \frac{\sqrt{2}}{2} \begin{bmatrix} 1 \\ 0 \\ 1 \end{bmatrix}, \quad (57b)$$

$$\hat{\mathbf{e}}_T^{\text{intermediate}} = -\frac{3\sqrt{2}}{2} \begin{bmatrix} 1 \\ 0 \\ 1 \end{bmatrix}, \quad (57c)$$

$$\hat{\mathbf{e}}_L^{\text{intermediate}} = -2\sqrt{2} \begin{bmatrix} 1 \\ 0 \\ 1 \end{bmatrix}, \quad (57d)$$

$$\hat{\mathbf{e}}^{\text{near}} = -\frac{9\sqrt{2}}{2} \begin{bmatrix} 1 \\ 0 \\ 1 \end{bmatrix}, \quad (57e)$$

$$\hat{\mathbf{h}}_T^{\text{far}} = \begin{bmatrix} 0 \\ 0 \\ 0 \end{bmatrix}, \quad (57f)$$

$$\hat{\mathbf{h}}_T^{\text{near}} = \begin{bmatrix} 0 \\ 0 \\ 0 \end{bmatrix}. \quad (57g)$$

The waveforms of u_1 , E_1 and H_2 are plotted in Fig. 15. In Fig. 15(a), we can see the P wave arriving at $t = 14$ s. The S wave that arrives at $t = 22$ s is weaker than the P wave. This is because: (1) as shown in eq. (57a), the far field of the S wave is zero; (2) meanwhile the intermediate and near fields of the S wave are smaller than the far field of the P wave at $r = 62$ km. In Fig. 15(b), we can see the electric field accompanying the P wave which arrives at $t = 14$ s. The electric field accompanying the S wave cannot be seen due to the weak amplitude and the weak electric-field-inducing capability of the S wave. In Fig. 15(b) it has been amplified by a factor 10 000 to be apparent. The electric field due to the EM wave is also amplified by a factor 10 000 can be seen. It is interesting that no magnetic field induced by the S or EM wave can be observed in Fig. 15(c). This is because both the far and near fields of the magnetic field are zero at point D.

The above discussions show that the recorded waveforms are sensitive to the observation orientation.

5 CONCLUSIONS AND DISCUSSIONS

We have derived the frequency-space-domain Green's function of the magnetic field for a point force as a complement of Pride & Haartsen (1996)'s work. Different from the electric field, which is a combination of all the four body waves, the magnetic field is only composed of the T mode waves (i.e. the S and EM waves). Furthermore, we extended the Green's functions of the elastic and EM wavefields to the moment tensor sources. As a frequently used source model in seismology, the double couple was taken for example and its radiation patterns were discussed. For the longitudinal mode waves, the shapes of the radiation patterns of the electric far field are similar to that of the P wave in elastodynamics. For the transverse mode waves, the shapes of radiation patterns of the electric and magnetic far fields are the same, and moreover, they are both identical to the S wave in elastodynamics. The near field of the EM wave has a longer dominant distance than the

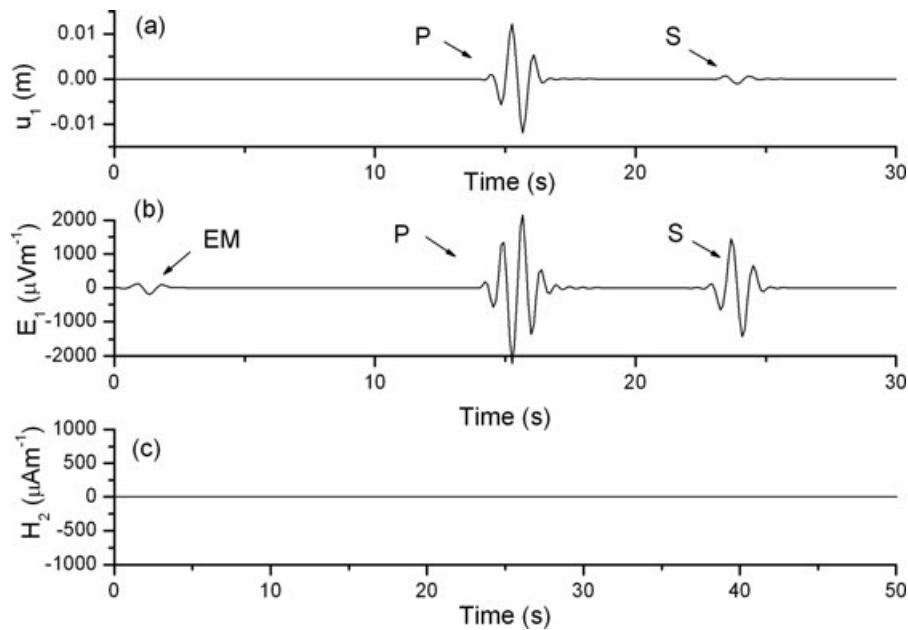


Figure 15. Waveforms of u_1 , E_1 and H_2 at point D. The electric fields due to the S and EM waves have been both amplified by a factor 10 000 in order to be apparent.

seismic waves. Such a near-field-domaining distance is sensitive to the salinity. We got the waveforms by Fourier transforming the Green's functions into the time domain. In order to check the validity of the Green's functions, we calculated the waveforms by another method that regarding the double couple source as a displacement–stress–EM discontinuity vector. It is shown that the waveforms calculated by the two methods agree with each other. We have simulated waveforms at three different observation points. In these waveforms, there is the electric field accompanying the P wave as well as the magnetic field accompanying the S wave. We have testified that the S wave usually has a weaker capacity than the P wave in inducing an electric field. The EM wave appears in both the electric and magnetic waveforms immediately after the source launched. It may be useful for the earthquake early warning due to its much higher speed compared with the seismic waves. However, it has much weaker amplitude than the accompanying electric and magnetic fields. Whether such an EM wave could be received and identified during an earthquake needs further studies. By making a comparison between the waveforms at different observation locations, we find that the waveforms are sensitive to the observation orientation.

The main purpose of this paper is to reveal the characteristics of the electric and magnetic fields radiated by a double couple source in an infinite uniform space. The boundary effect was not considered. However, when solving a physical problem in seismology, the boundary effect must be taken into account. To solve regular geological problems, a set of analytical formulas has been presented for horizontally stratified media (Haartsen & Pride 1997; Garambois & Dietrich 2002; White & Zhou 2006) and radially stratified formations (Hu & Liu 2002; Hu *et al.* 2007). To solve irregular geological problem, the finite-difference method has been developed (Guan & Hu 2008; Guan *et al.* 2009). Another efficient approach can be used to solve the coupled poroelastic and EM problem is the boundary element method (Ge & Chen 2007, 2008). The fundamental solutions obtained in the present paper are useful for such a method.

The equivalence between the fault slipping and the double couple source is under the hypothesis that the scale of the fault is much smaller than the wavelength considered. Otherwise, when the scale of the fault becomes comparable to or larger than the wavelength considered, the fault cannot be taken as a point source any longer. In this situation, such a fault can be divided into a series of small subfaults, each of which can be recognized as a double couple. The wavefields generated by the whole fault slip are a stacking of those generated by the subfaults, and can be calculated by an integral on the whole fault (Olson & Apsel 1982). These problems will be investigated in our further studies.

ACKNOWLEDGMENTS

This work is supported by the National Natural Science Foundation of China (Grant No. 40874062) and the Special Research Funds of Seismology in China (Grant No. 200808072).

REFERENCES

- Aki, K. & Richards, P.G., 2002. *Quantitative Seismology*, University Science Books Sausalito, California.
- Backus, G. & Mulcahy, M., 1976a. Moment tensors and other phenomenological descriptions of seismic sources: I. continuous displacements, *Geophys. J. Int.*, **46**(2), 341–361.
- Backus, G. & Mulcahy, M., 1976b. Moment tensors and other phenomenological descriptions of seismic sources: II. discontinuous displacements, *Geophys. J. Int.*, **47**(2), 301–329.
- Bonnet, G., 1987. Basic singular solutions for a poroelastic medium in the dynamic range, *J. acoust. Soc. Am.*, **82**(5), 1758–1762.
- Bordes, C., Jouniaux, L., Dietrich, M., Pozzi, J.-P. & Garambois, S., 2006. First laboratory measurements of seismo-magnetic conversions in fluid-filled Fontainebleau sand, *Geophys. Res. Lett.*, **33**, L01302.

- Bordes, C., Jouniaux, L., Garambois, S., Dietrich, M., Pozzi, J.-P. & Gaffet, S., 2008. Evidence of the theoretically predicted seismo-magnetic conversion, *Geophys. J. Int.*, **174**, 489–504.
- Boutin, C., 1991. Integral representation and sources in isotropic poroelastic media, in *Transport Processes in Porous Media*, pp. 521–538, eds Bear, J. & Corapcioglu, M.Y., Kluwer Academic Publishers, Dordrecht.
- Burridge, R. & Vargas, C., 1979. The fundamental solutions in dynamic poroelasticity, *Geophys. J. R. astr. Soc.*, **58**, 61–90.
- Butler, K.E., Russel, R.D., Kepic, A.W. & Maxwell, M., 1996. Measurement of the seismoelectric response from a shallow boundary, *Geophysics*, **61**, 1769–1778.
- Frenkel, J., 1944. On the theory of seismic and seismoelectric phenomena in a moist solid, *J. Phys. (Russian)*, **8**(4), 230–241.
- Garambois, S. & Dietrich, M., 2001. Seismoelectric wave conversions in porous media: field measurements and transfer function analysis, *Geophysics*, **66**, 1417–1430.
- Garambois, S. & Dietrich, M., 2002. Full waveform numerical simulations of seismoelectromagnetic wave conversions in fluid-saturated stratified porous media, *J. geophys. Res.*, **107**(B7), 2148, doi:10.1029/2001JB00316.
- Ge, Z. & Chen, X., 2007. Wave propagation in irregularly layered elastic models: a boundary element approach with a global reflection/transmission matrix propagator, *Bull. seism. Soc. Am.*, **97**(3), 1025–1031.
- Ge, Z. & Chen, X., 2008. An efficient approach for simulating wave propagation with the boundary element method in multilayered media with irregular interfaces, *Bull. seism. Soc. Am.*, **98**(6), 3007–3016.
- Guan, W. & Hu, H., 2008. Finite-difference modeling of electroseismic logging in a fluid saturated porous formation. *J. Comp. Phys.*, **228**, 5633–5648.
- Guan, W., Hu H. & He, X., 2009. Finite-difference modeling of the monopole acoustic logs in a horizontally stratified porous formation. *J. acoust. Soc. Am.*, **125**(4), 1942–1950.
- Haartsen, M.W. & Pride, S.R., 1997. Electroseismic waves from point sources in layered media, *J. geophys. Res.*, **102**, 24 745–24 769.
- Honkura, Y., Matsushima, M., Oshiman, N., Tuncer, M.K., Baris, S., Ito, A., Iio, Y. & Isikara, A.M., 2002. Small electric and magnetic signals observed before the arrival of seismic wave. *Earth Planets Space*, **54**, 9–12.
- Hu, H. & Gao, Y., 2009. The electric field induced by the fast P-wave and its nonexistence in a dynamically compatible porous medium, *SEG Technical Program Expanded Abstracts*, RP P1, 2170–2174.
- Hu, H., Guan, W. & Harris, J., 2007. Theoretical simulation of electroacoustic borehole logging in fluid-saturated porous formation, *J. acoust. Soc. Am.*, **122**, 135–145.
- Hu, H. & Liu, J., 2002. Simulation of the converted electric field during acoustoelectric logging, *SEG Technical Program Expanded Abstracts*, 1817–1820.
- Hu, H., Liu, J. & Wang, K., 2002. Attenuation and seismoelectric characteristics of dynamically compatible porous media, *SEG Technical Program Expanded Abstracts*, 1817–1820.
- Huang, Q., 2002. One possible generation mechanism of co-seismic electric signals, *Proc. Japan. Acad.*, **78**(B7), 173–178.
- Ivanov, A.G., 1939. Effect of electrization of earth layers by elastic waves passing through them, *Dokl. Akad. Nauk. SSSR*, **24**, 42–45.
- Karakelian, D., Beroza, G.C., Klemperer, S.L. & Fraser-Smith, A.C., 2002. Analysis of ultralow-frequency electromagnetic field measurements associated with the 1999 *M* 7.1 Hector Mine, California, Earthquake Sequence, *Bull. seism. Soc. Am.*, **92**, 1513–1524.
- Karpfinger, F., Müller T.M. & Gurevich, B., 2009. Green's functions and radiation patterns in poroelastic solids revisited. *Geophys. J. Int.*, **178**, 327–337.
- Kennett, B.L.N. & Kerry, N.J., 1979. Seismic waves in a stratified half space, *Geophys. J. R. astr. Soc.*, **57**, 557–583.
- Matsushima M. *et al.*, 2002. Seismoelectromagnetic effect associated with the Izmit earthquake and its aftershocks, *Bull. seism. Soc. Am.*, **92**, 350–360.
- Mikhailov, O.V., Haartsen, M.W. & Toksoz, M.N., 1997. Electroseismic investigation of the shallow subsurface: field measurements and numerical modeling, *Geophysics*, **62**, 97–105.
- Norris, A.N., 1985. Radiation from a point source and scattering theory in a fluid-saturated porous solid, *J. acoust. Soc. Am.*, **77**(6), 2012–2023.
- Olson, A.H. & Apsel, R.J., 1982. Finite faults and inverse theory with application to the 1979 Imperial Valley earthquake, *Bull. seism. Soc. Am.*, **72**(6), 1969–2001.
- Pengra, D.B., Sidney, X.L. & Wong, P., 1999. Determination of rock properties by low-frequency AC electrokinetics, *J. geophys. Res.*, **104**(B12), 29 485–29 508.
- Pride, S.R., 1994. Governing equations for the coupled electromagnetics and acoustics of porous media, *Phys. Rev. B*, **50**, 15 678–15 696.
- Pride, S.R. & Garambois, S., 2005. Electroseismic wave theory of Frenkel and more recent developments, *J. Engrg. Mech.*, **131**(9), 898–907.
- Pride, S.R. & Haartsen, M.W., 1996. Electroseismic wave properties. *J. acoust. Soc. Am.*, **100**, 1301–1315.
- Pujol, J., 2003. *Elastic Wave Propagation and Generation in Seismology*, Cambridge University Press, New York.
- Pride, S.R., Moreau, F. & Gavrilenko, P., 2004. Mechanical and electrical response due to fluid-pressure equilibration following an earthquake, *J. geophys. Res.*, **109**, B03302, doi:10.1029/2003.JB002690.
- Reppert, P.M. & Morgan, F.D., 2002. Frequency-Dependent Electroosmosis, *J. Colloid Interface Sci.*, **254**, 372–383.
- Tang, J. *et al.*, 2008. Coseismic signal associated with aftershock of the *M_s* 8.0 Wenchuan earthquake. *Seismol. Geol. (in Chinese)*, **30**(3), 739–745.
- Thompson, A.H. & Gist, G.A., 1993. Geophysical application of electrokinetic conversion, *Leading Edge*, **12**, 1169–1173.
- Vernik, L., 1998. Acoustic velocity and porosity systematics in siliciclastics. *Log Anal.*, **39**, 27–35.
- White, B.S. & Zhou, M., 2006. Electroseismic prospecting in layered media, *Soc. Indust. appl. Math.*, **67**(1), 69–98.
- Zhu, Z., Cheng, C.H. & Toksöz, M.N., 1994. Electro-kinetic conversion in a fluid-saturated porous rock sample, *SEG Technical Program Expanded Abstracts*, 1057–1060.
- Zhu, Z., Haartsen, M.W. & Toksöz, M.N., 1999. Experimental studies of electrokinetic conversions in fluid-saturated borehole models, *Geophysics*, **64**, 1349–1356.
- Zhu, Z., Toksöz, M.N. & Burns, D.R., 2008. Electroseismic and seismoelectric measurements of rock samples in a water tank, *Geophysics*, **73**, 153–164.

APPENDIX A: BULK WAVE SLOWNESSES AND COMPLEX AMPLITUDES OF THE GREEN'S FUNCTIONS

The slownesses of the compression waves are expressed as

$$2s_{pf,ps}^2 = \gamma \mp \sqrt{\gamma - \frac{4\tilde{\rho}\rho}{HM - C^2} \left(\frac{\rho_t}{\rho} + \frac{\tilde{\rho}L^2}{\tilde{\epsilon}} \right)}, \quad (\text{A1})$$

where the ‘−’ corresponds to the *Pf*-wave slowness s_{pf} while the ‘+’ corresponds to the *Ps*-wave slowness s_{ps} , and

$$\gamma = \frac{\rho M + \tilde{\rho}H(1 + \tilde{\rho}L^2/\tilde{\epsilon}) - 2\rho_f C}{HM - C^2}, \quad (\text{A2})$$

$$\rho_t = \rho - \rho_f^2 / \tilde{\rho}. \quad (\text{A3})$$

The slownesses of the transverse waves are

$$2s_{s,em}^2 = \frac{\rho_t}{G} + \mu\tilde{\varepsilon} \left(1 + \frac{\tilde{\rho}L^2}{\tilde{\varepsilon}}\right) \pm \left\{ \left[\frac{\rho_t}{G} - \mu\tilde{\varepsilon} \left(1 + \frac{\tilde{\rho}L^2}{\tilde{\varepsilon}}\right) \right]^2 - 4\mu \frac{\rho_f^2 L^2}{G} \right\}^{1/2}, \quad (\text{A4})$$

where, the ‘+’ in front of radical corresponds to the *S* wave while the ‘−’ corresponds to the *EM* wave. The expressions of the complex amplitudes of the Green’s functions in eq. (22) have been derived by Pride & Haartsen (1996). Here we only list the ones corresponding to the force acting on the bulk material **F**. They are necessary for the calculation in the main text.

$$T_{u,s_s}^F = \frac{s_s^2 - \mu\tilde{\varepsilon}(1 + \tilde{\rho}L^2/\tilde{\varepsilon})}{G(s_s^2 - s_{em}^2)}, \quad (\text{A5})$$

$$T_{u,s_{em}}^F = \frac{s_{em}^2 - \mu\tilde{\varepsilon}(1 + \tilde{\rho}L^2/\tilde{\varepsilon})}{G(s_{em}^2 - s_s^2)}, \quad (\text{A6})$$

$$L_{u,s_{pf}}^F = \left(\frac{M}{HM - C^2} \right) \frac{s_{pf}^2 - \tilde{\rho}(1 + \tilde{\rho}L^2/\tilde{\varepsilon})M}{(s_{pf}^2 - s_{ps}^2)}, \quad (\text{A7})$$

$$L_{u,s_{ps}}^F = \left(\frac{M}{HM - C^2} \right) \frac{s_{ps}^2 - \tilde{\rho}(1 + \tilde{\rho}L^2/\tilde{\varepsilon})M}{(s_{ps}^2 - s_{pf}^2)}, \quad (\text{A8})$$

$$T_{w,s_s}^F = -\frac{\rho_f}{\tilde{\rho}} \frac{s_s^2 - \mu\tilde{\varepsilon}}{G(s_s^2 - s_{em}^2)}, \quad (\text{A9})$$

$$T_{w,s_{em}}^F = -\frac{\rho_f}{\tilde{\rho}} \frac{s_{em}^2 - \mu\tilde{\varepsilon}}{G(s_{em}^2 - s_s^2)}, \quad (\text{A10})$$

$$L_{w,s_{pf}}^F = -\frac{M}{HM - C^2} \frac{s_{pf}^2 - \rho_f/C}{(s_{pf}^2 - s_{ps}^2)}, \quad (\text{A11})$$

$$L_{w,s_{ps}}^F = -\frac{M}{HM - C^2} \frac{s_{ps}^2 - \rho_f/C}{(s_{ps}^2 - s_{pf}^2)}, \quad (\text{A12})$$

$$T_{E,s_s}^F = \frac{i\omega\mu\rho_f L}{G(s_s^2 - s_{em}^2)}, \quad (\text{A13})$$

$$T_{E,s_{em}}^F = \frac{i\omega\mu\rho_f L}{G(s_{em}^2 - s_s^2)}, \quad (\text{A14})$$

$$L_{E,s_{pf}}^F = -i\omega \frac{\tilde{\rho}L}{\tilde{\varepsilon}} \left(\frac{M}{HM - C^2} \right) \frac{s_{pf}^2 - \rho_f/C}{(s_{pf}^2 - s_{ps}^2)}, \quad (\text{A15})$$

$$L_{E,s_{ps}}^F = -i\omega \frac{\tilde{\rho}L}{\tilde{\varepsilon}} \left(\frac{M}{HM - C^2} \right) \frac{s_{ps}^2 - \rho_f/C}{(s_{ps}^2 - s_{pf}^2)}, \quad (\text{A16})$$

APPENDIX B: PROOF OF EQ. (25)

The eq. (25) can be rewritten as

$$\nabla \times \left[\underbrace{\mathbf{e}^{i\omega sr} \left(-\frac{1}{r} - \frac{3i}{\omega sr^2} + \frac{3}{\omega^2 s^2 r^3} \right)}_{f(r)} \underbrace{\hat{\mathbf{r}}}_{\mathbf{A}} + \underbrace{\mathbf{e}^{i\omega sr} \left(\frac{i}{\omega sr^2} - \frac{1}{\omega^2 s^2 r^3} \right)}_{g(r)} \mathbf{I} \right] = 0. \quad (\text{B1})$$

Note that

$$\nabla \times [X(r)\mathbf{Y}] = \nabla X(r) \times \mathbf{Y} + X(r)\nabla \times \mathbf{Y} = X'(r)\hat{\mathbf{r}}_k Y_{ij} \varepsilon_{kil} \mathbf{e}_i \mathbf{e}_j + X(r) \frac{\partial Y_{ij}}{\partial x_k} \varepsilon_{kil} \mathbf{e}_i \mathbf{e}_j. \quad (\text{B2})$$

In eq. (B2), $X(r)$ is a scalar function of r , \mathbf{Y} is a tensorial function, ε_{kil} is the permutation symbol, and here the Einstein summation convention is used. Using the notations of (B1), we obtain

$$\begin{aligned}\nabla \times [f(r)\mathbf{A}] &= e^{i\omega s r} \left(-\frac{i\omega s}{r} + \frac{4}{r^2} + \frac{9i}{\omega s r^3} - \frac{9}{\omega^2 s^2 r^4} \right) \hat{r}_k \hat{r}_i \hat{r}_j \varepsilon_{kil} \mathbf{e}_l \mathbf{e}_j \\ &\quad + e^{i\omega s r} \left(-\frac{1}{r^2} - \frac{3i}{\omega s r^3} + \frac{3}{\omega^2 s^2 r^4} \right) (\hat{r}_i \delta_{jk} + \hat{r}_j \delta_{ik} - 2\hat{r}_k \hat{r}_i \hat{r}_j) \varepsilon_{kil} \mathbf{e}_l \mathbf{e}_j \\ &= e^{i\omega s r} \left(-\frac{1}{r^2} - \frac{3i}{\omega s r^3} + \frac{3}{\omega^2 s^2 r^4} \right) \hat{r}_i \varepsilon_{jil} \mathbf{e}_l \mathbf{e}_j,\end{aligned}\quad (\text{B3})$$

where δ_{jk} is the Kronecker delta symbol. During the derivation of (B3), the following relations

$$\frac{\partial \hat{r}_i}{\partial x_j} = \frac{\delta_{ij} - \hat{r}_i \hat{r}_j}{r}, \quad (\text{B4})$$

$$\hat{r}_k \hat{r}_i \varepsilon_{kil} = 0, \quad (\text{B5})$$

$$\hat{r}_j \delta_{ik} \varepsilon_{kil} = 0, \quad (\text{B6})$$

are used. Similarly, we have

$$\nabla \times [g(r)\mathbf{I}] = e^{i\omega s r} \left(-\frac{1}{r^2} - \frac{3i}{\omega s r^3} + \frac{3}{\omega^2 s^2 r^4} \right) \hat{r}_i \varepsilon_{ijl} \mathbf{e}_l \mathbf{e}_j. \quad (\text{B7})$$

At last, combining eq. (B3) and (B7), and using the relation

$$\varepsilon_{ijl} = -\varepsilon_{jil}, \quad (\text{B8})$$

we finally get

$$\nabla \times [f(r)\mathbf{A} + g(r)\mathbf{I}] = 0. \quad (\text{B9})$$

Then the eq. (B1) comes into existence.

APPENDIX C: COMPARISON OF ELECTRIC-FIELD-INDUCING ABILITIES BETWEEN THE P AND S WAVES

Garambois & Dietrich (2001) derived the low-frequency approximate seismoelectric and seismomagnetic transfer functions

$$\mathbf{E} \approx \frac{1}{\sigma_f} \frac{\varepsilon_0 \rho_f \kappa_f \zeta}{\eta} \left(1 - \frac{\rho C}{\rho_f H} \right) \ddot{\mathbf{u}}, \quad (\text{C1})$$

$$|\mathbf{H}| \approx \frac{\phi}{\alpha_\infty} \frac{\varepsilon_0 \rho_f \kappa_f |\zeta|}{\eta} \sqrt{\frac{G}{\rho}} |\dot{\mathbf{u}}|. \quad (\text{C2})$$

where ε_0 is the vacuum's dielectric permittivity, ρ_f is the fluid density, κ_f and σ_f represent the fluid's dielectric constant and electric conductivity, ζ denotes the zeta potential, η is the fluid viscosity, ρ is the bulk density, H and C are the elastic moduli expressed in the eqs (7) and (8) in the main text. ϕ is the porosity, α_∞ is the tortuosity, $\ddot{\mathbf{u}}$ and $\dot{\mathbf{u}}$ are the grain acceleration and velocity, respectively. According to eqs (C1) and (C2), we have

$$|\mathbf{E}|^P \approx \frac{1}{\sigma_f} \frac{\varepsilon_0 \rho_f \kappa_f |\zeta| \omega^2}{\eta} \left(1 - \frac{\rho C}{\rho_f H} \right) |\mathbf{u}|^P, \quad (\text{C3})$$

$$|\mathbf{H}|^S \approx \frac{\phi}{\alpha_\infty} \frac{\varepsilon_0 \rho_f \kappa_f |\zeta| \omega}{\eta} \sqrt{\frac{G}{\rho}} |\mathbf{u}|^S, \quad (\text{C4})$$

where $|\mathbf{E}|^P$ and $|\mathbf{u}|^P$ denote the electric field and the solid displacement corresponding to a P wave, while $|\mathbf{E}|^S$ and $|\mathbf{u}|^S$ denote the electric field and the solid displacement corresponding to an S wave. Using the relation

$$\mathbf{H} = \frac{1}{i\omega\mu} \nabla \times \mathbf{E}, \quad (\text{C5})$$

in the frequency domain, we have

$$|\mathbf{H}| = \left| \frac{i\omega s}{i\omega\mu} \mathbf{E} \right| = \frac{s}{\mu} |\mathbf{E}|, \quad (\text{C6})$$

where s is the slowness of the body wave, μ is the magnetic permeability. Then using the eqs (C6) and (C4), we get the expression of the electric field accompanying the S wave

$$|\mathbf{E}|^S = \frac{\mu}{s_s} |\mathbf{H}|^S \approx \frac{\phi}{\alpha_\infty} \frac{\varepsilon_0 \rho_f \kappa_f |\zeta| \omega}{\eta} \sqrt{\frac{G}{\rho}} \frac{\mu}{s_s} |\mathbf{u}|^S, \quad (\text{C7})$$

where s_s is the slowness of the S wave, and in the low frequency range, its approximate expression (Garambois & Dietrich 2001) is

$$s_s = \sqrt{\frac{\rho}{G}}. \quad (C8)$$

Dividing eq. (C7) by eq. (C3), we get the ratio of electric field induced by an S wave to that induced by a P wave

$$\frac{|\mathbf{E}|^S}{|\mathbf{E}|^P} = \frac{\phi \sigma_f \mu G}{\alpha_\infty \rho \left(1 - \frac{\rho C}{\rho_f H}\right) \omega} \frac{|\mathbf{u}|^S}{|\mathbf{u}|^P}. \quad (C9)$$

The fluid electric conductivity σ_f is defined as Pride (1994)

$$\sigma_f = e^2 z^2 N (b_+ + b_-), \quad (C10)$$

where $e = 1.6021892 \times 10^{-19}$ C is the electronic charge, $z = 1$ is the ionic valence, b_\pm are the ionic mobilities of the cations and anions. Here we choose $b_+ = b_- = 3 \times 10^{11}$ m s⁻¹ N as Pride (1994). N is the ionic concentration in ions per meters cubed and is defined as

$$N = 6.022 \times 10^{26} C_0, \quad (C11)$$

where C_0 is the salinity. Then, we obtain

$$\sigma_f = 9.27512 C_0. \quad (C12)$$

Using eq. (C9) and the parameters in Table 1, we have

$$\frac{|\mathbf{E}|^S}{|\mathbf{E}|^P} = \frac{0.0011}{f} \frac{|\mathbf{u}|^S}{|\mathbf{u}|^P}. \quad (C13)$$

In this paper, the centre frequency is $f_0 = 1$ Hz, and the frequency varies from 0.1 to 1.9 Hz. Then, we get

$$0.00058 \frac{|\mathbf{u}|^S}{|\mathbf{u}|^P} \leq \frac{|\mathbf{E}|^S}{|\mathbf{E}|^P} \leq 0.011 \frac{|\mathbf{u}|^S}{|\mathbf{u}|^P}. \quad (C14)$$

From eq. (C14), we know that if $|\mathbf{u}|^S = |\mathbf{u}|^P$, $|\mathbf{E}|^S$ is much smaller than $|\mathbf{E}|^P$. This means the S wave has a much weaker capacity in inducing electric field than the P wave. From Fig. 10, we get $u_{1 \max}^P = 0.0077$ m, $u_{1 \max}^S = 0.0137$ m, $u_{2 \max}^P = 1.25 \times 10^{-4}$ m, $u_{2 \max}^S = 4.6 \times 10^{-4}$ m, $u_{3 \max}^P = 0.002$ m and $u_{3 \max}^S = 0.053$ m. Then, we have

$$0.0011 \leq \frac{E_{1 \max}^S}{E_{1 \max}^P} \leq 0.02, \quad (C15)$$

$$0.0022 \leq \frac{E_{2 \max}^S}{E_{2 \max}^P} \leq 0.041, \quad (C16)$$

$$0.0153 \leq \frac{E_{3 \max}^S}{E_{3 \max}^P} \leq 0.29. \quad (C17)$$

Finally, as illustrated in Fig. 11, we find that $|\mathbf{E}|^S$ is much less than $|\mathbf{E}|^P$ in our numerical simulations.

However, this conclusion must be considered carefully. From eq. (C9) we know that the term $(1 - \rho C / \rho_f H)$ influences the ratio $|\mathbf{E}|^S / |\mathbf{E}|^P$, and in our calculation $(1 - \rho C / \rho_f H) \approx 0.6$. In most cases, $(1 - \rho C / \rho_f H)$ approximates 1 (Garambois & Dietrich 2001) and makes a negligible impact on the ratio $|\mathbf{E}|^S / |\mathbf{E}|^P$. But such approximation is not valid in some special media. Using Vernik's (1998) relations between frame moduli and porosity, Hu *et al.* (2002) showed that for certain real sedimentary rocks, the value of the term $(1 - \rho C / \rho_f H)$ can be very small or even zero. In this instance, $(1 - \rho C / \rho_f H)$ will make a great impact on the ratio $|\mathbf{E}|^S / |\mathbf{E}|^P$, and $|\mathbf{E}|^S$ may exceed $|\mathbf{E}|^P$. When $(1 - \rho C / \rho_f H) = 0$, the porous medium becomes a dynamically compatible medium, in which the P wave does not induce any electric field. This phenomenon has been discussed in detail by Hu & Gao (2009).

APPENDIX D: DERIVATION OF THE DISPLACEMENT-STRESS-EM DISCONTINUITY VECTOR FOR A DOUBLE COUPLE SOURCE

To solve the wavefields in a horizontally stratified formation, a cylindrical-coordinate system (r, θ, z) with z indicating the depth is convenient because the stratified media are axisymmetric and the point sources are assumed. We represent the field variable ξ in terms of the vector surface harmonics (Kennett & Kerry 1979; Haartsen & Pride 1997)

$$\mathbf{R}_k^m(r, \theta) = J_m(kr) e^{im\theta} \mathbf{e}_z, \quad (D1a)$$

$$\mathbf{S}_k^m(r, \theta) = -i J_m'(kr) e^{im\theta} \mathbf{e}_r + \frac{m}{kr} J_m(kr) e^{im\theta} \mathbf{e}_\theta, \quad (D1b)$$

$$\mathbf{T}_k^m(r, \theta) = \frac{m}{kr} J_m(kr) e^{im\theta} \mathbf{e}_r + i J_m'(kr) e^{im\theta} \mathbf{e}_\theta, \quad (D1c)$$

as a Fourier–Hankel transform

$$\begin{aligned}\xi(r, \theta, z, \omega) &= \xi_r(r, \theta, z, \omega)\mathbf{e}_r + \xi_\theta(r, \theta, z, \omega)\mathbf{e}_\theta + \xi_z(r, \theta, z, \omega)\mathbf{e}_z \\ &= \int_{-\infty}^{+\infty} dk \sum_m \left[\hat{\xi}_1(k, m, z, \omega)\mathbf{S}_k^m + \hat{\xi}_2(k, m, z, \omega)\mathbf{T}_k^m + \hat{\xi}_z(k, m, z, \omega)\mathbf{R}_k^m \right],\end{aligned}\quad (\text{D2})$$

where $J_m(kr)$ is the m -order Bessel function of the first kind, $J'_m(kr) = \frac{1}{k} \frac{dJ_m(kr)}{dr}$, k is the horizontal wavenumber, $\mathbf{e}_r, \mathbf{e}_\theta$ and \mathbf{e}_z are the coordinate unit vectors. The field vector ξ can be $\mathbf{u}, \mathbf{w}, \mathbf{E}, \mathbf{H}, \mathbf{t}, \mathbf{F}, \mathbf{C}$ or \mathbf{M} . $\mathbf{t} = \tau_{rz}\mathbf{e}_r + \tau_{\theta z}\mathbf{e}_\theta + \tau_{zz}\mathbf{e}_z$ represents the force vector in a horizontal plane, m is chosen as ± 1 for the double couple. $\hat{\xi}$ is the field vector in the new coordinates composed of $\mathbf{R}_k^m, \mathbf{S}_k^m$ and \mathbf{T}_k^m . The Pride's eqs (1)–(6) are then transformed to

$$\frac{\partial}{\partial z} \mathbf{B}(k, m, z, \omega) = \mathbf{A}(k, \omega) \mathbf{B}(k, m, z, \omega) + \bar{\mathbf{F}}(k, z, \omega), \quad (\text{D3})$$

where \mathbf{B} denotes the displacement–stress–EM vector, $\bar{\mathbf{F}}$ denotes the source vector. The mark ‘ $-$ ’ on the top of $\bar{\mathbf{F}}$ is used to distinguish from \mathbf{F} , which represents the body force acting on the bulk material in eq. (3). \mathbf{A} is a matrix dependent on the frequency ω , the wavenumber k and the parameters of the porous formation. One can get the detailed expression of \mathbf{A} in Haartsen & Pride (1997). The set of equations shown in (D3) is then split into two independent systems. One is the PSVTM set coupling the Pf, Ps, SV and TM waves. The other is the SHTE set coupling the SH and TE waves. The vectors \mathbf{B} in the two systems are written as

$$\mathbf{B}^V = [\hat{u}_1, \hat{u}_z, \hat{w}_z, \hat{\tau}_{1z}, \hat{\tau}_{zz}, -P, \hat{E}_1, \hat{H}_2]^T, \quad (\text{D4})$$

$$\mathbf{B}^H = [\hat{u}_2, \hat{\tau}_{2z}, \hat{E}_2, \hat{H}_1]^T. \quad (\text{D5})$$

The superscripts ‘V’ and ‘H’ correspond to the PSVTM system and the SHTE system, respectively. The source vectors $\bar{\mathbf{F}}$ in the two systems are

$$\bar{\mathbf{F}}^V = \left[0, 0, \frac{ip}{\omega\bar{\rho}} \hat{f}_1, \frac{\rho_f}{\bar{\rho}} \hat{f} - \hat{F}_1, -\hat{F}_z, -\hat{f}_z + \frac{\bar{\rho}L}{\bar{\varepsilon}} \hat{C}_z, -L \hat{f}_1 - \hat{C}_1, \frac{p}{\bar{\varepsilon}} \hat{C}_z - \hat{M}_2 \right]^T, \quad (\text{D6})$$

$$\bar{\mathbf{F}}^H = \left[0, \frac{\rho_f}{\bar{\rho}} \hat{f}_2, L \hat{f}_2 + \hat{C}_2 - \frac{p}{\mu} \hat{M}_z, \hat{M}_1 \right]^T, \quad (\text{D7})$$

where the superscript ‘ T ’ denotes the transpose.

At the interface with depth z separating two different porous layers, the boundary condition requires

$$\mathbf{B}(z^-) = \mathbf{B}(z^+). \quad (\text{D8})$$

At the horizontal plane with depth z_s where the source locates, the vector \mathbf{B} is not continuous, and the discontinuity is

$$\mathbf{S} \equiv \mathbf{B}(z_s^+) - \mathbf{B}(z_s^-) = \bar{\mathbf{G}} + \mathbf{A}\bar{\mathbf{H}}, \quad (\text{D9})$$

where \mathbf{S} is the so-called displacement–stress–EM discontinuity vector for the source. $\bar{\mathbf{G}}$ and $\bar{\mathbf{H}}$ can be obtained from

$$\bar{\mathbf{F}} = \bar{\mathbf{G}}\delta(z - z_s) + \bar{\mathbf{H}} \frac{\partial}{\partial z} \delta(z - z_s). \quad (\text{D10})$$

From eqs (D6) and (D7), we know $\bar{\mathbf{F}}$ depends on $\hat{\mathbf{f}}$ and $\hat{\mathbf{F}}$. It can be obtained by following process.

According to the equivalence between the displacement–stress–EM vector discontinuity and the body force density at the source location, the source can be represented as

$$\mathbf{F}_e = -\nabla[\mathbf{M}\delta(\mathbf{r} - \mathbf{r}_s)], \quad (\text{D11})$$

where \mathbf{F}_e is the body force density as an equivalent of the moment tensor \mathbf{M} . In this paper, we assume that only the force acting on the bulk material exists while the force acting on the fluid phase is absent for the double couple source. Therefore, we set $\mathbf{F} = \mathbf{F}_e$ and $\mathbf{f} = 0$ in the Pride's equations (1)–(6). Using expression (D2), \mathbf{F} can be expressed as

$$\mathbf{F} = \int_0^{+\infty} dk \sum_m \left(\hat{F}_1 \mathbf{S}_k^m + \hat{F}_2 \mathbf{T}_k^m + \hat{F}_z \mathbf{R}_k^m \right). \quad (\text{D12})$$

And inversely, we have

$$\hat{F}_1 = \frac{1}{2\pi} \int_0^{+\infty} r dr \int_0^{2\pi} d\theta [\mathbf{S}_k^m]^* \cdot \mathbf{F}, \quad (\text{D13})$$

$$\hat{F}_2 = \frac{1}{2\pi} \int_0^{+\infty} r dr \int_0^{2\pi} d\theta [\mathbf{T}_k^m]^* \cdot \mathbf{F}, \quad (\text{D14})$$

$$\hat{F}_z = \frac{1}{2\pi} \int_0^{+\infty} r dr \int_0^{2\pi} d\theta [\mathbf{R}_k^m]^* \cdot \mathbf{F}, \quad (\text{D15})$$

where $*$ denotes the complex conjugate.

Consider a double couple in Cartesian coordinates

$$\mathbf{M}(x_1, x_2, x_3) = \begin{bmatrix} 0 & 0 & M_0 \\ 0 & 0 & 0 \\ M_0 & 0 & 0 \end{bmatrix}. \quad (\text{D16})$$

When transforming it into the cylindrical coordinates (r, θ, z) , we have

$$\mathbf{M}(r, \theta, z) = M_0 \begin{bmatrix} 0 & 0 & \cos \theta \\ 0 & 0 & -\sin \theta \\ \cos \theta & -\sin \theta & 0 \end{bmatrix}. \quad (\text{D17})$$

Substituting eq. (D17) into (D11), and adding the source frequency spectrum $s(\omega)$, we obtain

$$F_r = -M_0 \cos \theta s(\omega) \frac{\delta(r)}{r} \delta(\theta) \frac{\partial \delta(z - z_s)}{\partial z}, \quad (\text{D18})$$

$$F_\theta = M_0 \sin \theta s(\omega) \frac{\delta(r)}{r} \delta(\theta) \frac{\partial \delta(z - z_s)}{\partial z}, \quad (\text{D19})$$

$$F_z = M_0 s(\omega) \left\{ -\left[\frac{1}{r} \frac{\partial \delta(r)}{\partial r} - \frac{\delta(r)}{r^2} \right] \delta(\theta) \cos \theta + \frac{\delta(r)}{r^2} \frac{\partial \delta(\theta)}{\partial \theta} \sin \theta \right\} \delta(z - z_s). \quad (\text{D20})$$

Using the eqs (D13)–(D15), we get

$$\hat{F}_1 = \mp \frac{i M_0}{2} \frac{s(\omega)}{2\pi} \frac{\partial \delta(z - z_s)}{\partial z}, \quad (\text{D21})$$

$$\hat{F}_2 = -\frac{M_0}{2} \frac{s(\omega)}{2\pi} \frac{\partial \delta(z - z_s)}{\partial z}, \quad (\text{D22})$$

$$\hat{F}_z = \pm \frac{k M_0}{2} \frac{s(\omega)}{2\pi} \delta(z - z_s). \quad (\text{D23})$$

Substituting eqs (D21)–(D23) into (D6)–(D7), and using eq. (10), we obtain

$$\tilde{\mathbf{G}}^V = \frac{s(\omega)}{2\pi} M_0 \left[0, 0, 0, 0, \mp \frac{k}{2}, 0, 0, 0 \right]^T, \quad (\text{D24})$$

$$\tilde{\mathbf{H}}^V = \frac{s(\omega)}{2\pi} M_0 \left[0, 0, 0, \pm \frac{i}{2}, 0, 0, 0, 0 \right]^T, \quad (\text{D25})$$

and

$$\tilde{\mathbf{G}}^H = [0, 0, 0, 0]^T, \quad (\text{D26})$$

$$\tilde{\mathbf{H}}^H = \frac{s(\omega)}{2\pi} \frac{M_0}{2} [0, 1, 0, 0]^T. \quad (\text{D27})$$

Substituting eqs (24)–(27) into (D9), we finally have

$$\mathbf{S}^V = \frac{s_0(\omega)}{2\pi} M_0 \left[\pm \frac{i}{2G}, 0, 0, 0, 0, 0, 0, 0 \right]^T, \quad (\text{D28})$$

$$\mathbf{S}^H = \frac{s_0(\omega)}{2\pi} M_0 \left[\frac{1}{2G}, 0, 0, 0 \right]^T. \quad (\text{D29})$$

Similarly, for the double couple $M_{23} = M_{32} = M_0$, the displacement–stress–EM discontinuity vectors are

$$\mathbf{S}^V = \frac{s_0(\omega)}{2\pi} M_0 \left[\frac{1}{2G}, 0, 0, 0, 0, 0, 0, 0 \right]^T, \quad (\text{D30})$$

$$\mathbf{S}^H = \frac{s_0(\omega)}{2\pi} M_0 \left[\mp \frac{i}{2G}, 0, 0, 0 \right]^T. \quad (\text{D31})$$